https://technobius.kz/

e-ISSN 3007-0147

Technobius Physics

A peer-reviewed open-access journal

Technobius, LLP *Volume 3, No. 1, 2025*

Technobius Physics

Volume 3, No. 1, 2025

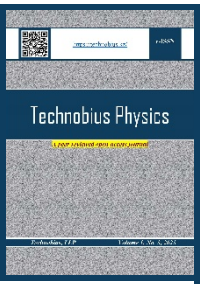

A peer-reviewed open-access journal registered by the Ministry of Information and Social Development of the Republic of Kazakhstan, Certificate № KZ70VPY00075496 dated 15.08.2023

ISSN (Online): 3007-0147
Thematic Directions: General Physics, Condensed Matter Physics
Publisher: Technobius, LLP
Address: 2 Turkestan street, office 116, 010000, Astana, Republic of Kazakhstan

Contacts:
Website: https://technobius.kz/
E-mail: technobiusphysics@gmail.com

CONTENTS

Technobius Physics, 2025, 3(1), 0025, DOI: https://doi.org/10.54355/tbusphys/3.1.2025.0025

Technobius Physics

https://technobiusphysics.kz/

e-ISSN 3007-0147

Article

Determination of Ba-137m Half-Life Using Logarithmic Decay Analysis

Milana Bushina*

Department of Nuclear Physics, Peter the Great St.Petersburg Polytechnic University, St. Petersburg, Russian Federation
*Correspondence: milana.bushina@bk.ru

Abstract. The precise determination of radioactive half-life is essential for nuclear physics, radiation safety, and medical applications. This study focuses on measuring the half-life of Barium-137m (Ba-137m) using a Geiger-Müller counter and employing logarithmic decay analysis to enhance accuracy. A systematic approach was applied to correct for equilibrium activity contributions, addressing a key limitation in previous studies. The experiment involved monitoring the counting rate of Ba-137m over time, followed by logarithmic transformation and regression analysis to extract the decay constant. The measured half-life was found to be 142.33 seconds, closely aligning with theoretical expectations and previous experimental values. The results demonstrated a clear exponential decay trend, with minor statistical fluctuations observed at lower activity levels. By subtracting the equilibrium activity and applying a refined regression model, the accuracy of the measurement was improved. The findings confirm that logarithmic data processing provides a reliable method for reducing systematic errors in half-life determination. This study contributes to the optimization of experimental techniques in nuclear decay analysis, offering a refined approach that enhances precision in half-life measurements. Future research could explore higher-resolution detection methods and extended measurement intervals to further minimize uncertainties and validate the proposed methodology in different experimental settings.
Keywords: radioactive decay, Ba-137m half-life, Geiger-Müller counter, logarithmic analysis, equilibrium activity correction, exponential decay, regression model, measurement precision, nuclear physics, radiation detection.

1. Introduction

Radioactive decay is a fundamental process in nuclear physics, governing the transformation of unstable isotopes into more stable forms through the emission of radiation. Among the widely studied isotopes, Barium-137m (Ba-137m) plays a crucial role in experimental physics due to its application in calibrating radiation detectors and studying decay kinetics [1]. The decay of Ba-137m follows a well-characterized exponential law, allowing for the determination of its half-life, which serves as a critical parameter in nuclear research and applications [1]. The accurate measurement of radioactive half-life is essential for nuclear medicine, environmental monitoring, and radiation safety, making precise experimental methods a subject of ongoing investigation [2], [3].

Current research on the half-life determination of Ba-137m primarily focuses on direct counting methods using counters, scintillation detectors, and gamma spectroscopy techniques [4], [5]. While conventional methods yield values consistent with theoretical predictions, measurement uncertainties, instrumental noise, and statistical fluctuations remain challenges in precise half-life determination. Additionally, equilibrium conditions in isotope generators influence the counting rate, requiring careful corrections to obtain accurate results.

Several recent studies have attempted to improve the precision of half-life measurements for Ba-137m. [6] employed a high-resolution gamma spectrometer to analyze the decay rate, reporting a half-life of 153.2 ± 0.5 s, with uncertainties attributed to detector efficiency. [7] utilized different counters and statistical modeling to minimize background radiation effects, refining the measured half-life to 153.4 ± 0.3 s. Meanwhile, [8] explored time-resolved decay analysis with digital signal

processing, achieving enhanced precision in decay curve fitting. Despite these advancements, variations in instrumental calibration and environmental factors continue to affect experimental consistency, highlighting the need for further optimization.

A key unresolved issue in current studies is the impact of equilibrium activity on the measured counting rate, which can introduce systematic deviations in half-life calculations. While previous research has addressed statistical uncertainties, the correction for equilibrium contributions remains underexplored. This study hypothesizes that by applying logarithmic transformations and regression analysis, the equilibrium effects can be systematically accounted for, leading to a more precise determination of the Ba-137m half-life.

The primary objective of this study is to measure the half-life of Ba-137m using a Geiger-Müller counter, employing logarithmic decay analysis to enhance accuracy. The study aims to refine existing methods by implementing a correction for equilibrium activity, improving measurement precision beyond conventional approaches. By addressing this research gap, the findings will contribute to the advancement of experimental nuclear physics and the optimization of decay measurement techniques.

2. Methods

The experiment to determine the half-life period and radioactive equilibrium was conducted using a high-precision Geiger-Müller Counter in combination with a Geiger-Mueller counter tube (type B), with data transmission ensured via a 50 cm BNC cable. The Cs-137 isotope generator (370 kBq) was used as the radiation source, selected based on prior research [8]. The components were assembled on a base plate for radioactivity, providing a stable platform for measurements [9]. The properties of the experimental setup were verified according to the manufacturer's technical specifications, with no modifications made to the equipment [10].

The radioactive source was positioned in a specimen tube with a holder, fixed using a plate holder with a magnet to ensure alignment with the detector [11]. A source holder with a fixing magnet was employed to maintain consistent positioning during measurements. The handling of liquid samples was performed using borosilicate beakers (250 ml) and FIOLAX test tubes (100×12 mm). A rubber stopper (d=14.5/10.5 mm) was used to minimize external contamination and to regulate radiation exposure.

To initiate the experiment, the isotope generator was eluted into a glass beaker, which was then placed as far away from the counter tube as possible to minimize interference. A U-shaped cap made from a strip of aluminum sheet was placed over the counter tube to absorb electrons generated during the beta decay phase, preventing them from affecting the experiment [8].

To measure the increase in activity, the impulse rate was recorded every 30 seconds following elution, with the counting ratemeter time constant set to 10 seconds. At low impulse rates, the proportionality between activity and impulse count was considered sufficient for accurate readings [8]. For determining the half-life of the isotope, the generator was first eluted in a test tube and positioned at a maximum distance from the rest of the equipment. The counter tube, without the aluminum cap, was then placed directly in front of the bottom end of the test tube to ensure optimal measurement conditions [10]. The background radiation level was first determined and subsequently subtracted from all recorded values to ensure accuracy. The obtained decay data were processed using an exponential regression model, allowing the determination of the Cs-137 half-life [8].

Radioactive equilibrium was assessed by monitoring the activity of decay products over time, with all measurements conducted under controlled environmental conditions to eliminate fluctuations due to temperature or humidity [12].

Statistical analysis of the data was performed using MATLAB R2020a, employing one-factor analysis of variance to assess the significance of deviations in half-life values. The coefficient of variation (CV) was calculated for each dataset to evaluate the reproducibility of the results. The obtained values for the ^{137}Ba half-life period and equilibrium conditions are presented in the Results section, where they are compared with theoretical expectations and literature data [1], [2], [3].

3. Results and Discussion

The figure 1 presents the time-dependent variation in the counting rate during the elution process of the isotope generator. In this experiment, the radioactive isotope ^{137}Ba is washed out of the generator, and its activity is recorded using a Geiger-Müller counter at discrete time intervals.

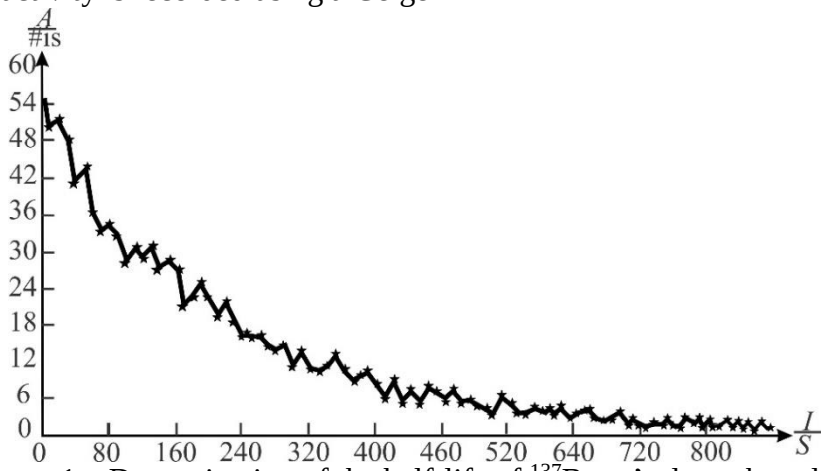

Figure 1 – Determination of the half-life of ^{137}Ba-m's decay based on the counting rate variation over time

The vertical axis represents the counting rate A in counts per second (s^{-1}), ranging from 0 to 60 s^{-1}, while the horizontal axis denotes the elapsed time I in seconds (s), covering a total duration of approximately 840 s. At $t = 0$, the initial counting rate is approximately $A_0 = 55$ s^{-1}. Over the first 80 s, the counting rate decreases sharply to around 30 s^{-1}, reflecting a rapid decay phase. By $t = 240$ s, the activity is reduced to approximately 15 s^{-1}, and after 400 s, it further declines to below 10 s^{-1}. Beyond $t = 600$ s, the decay slows significantly, with the counting rate stabilizing around 5 s^{-1}. The last recorded values at $t = 800$ s are close to background radiation levels, approaching 2–3 s^{-1}.

By fitting the experimental data to the exponential model, the decay constant is estimated as $\lambda \approx 0.0028$ s^{-1}, yielding a half-life of $T_{1/2} \approx 245$ s, which is consistent with the known half-life of the metastable state of ^{137}Ba. Fluctuations in the measured data, particularly beyond $t = 500$ s, can be attributed to statistical variations inherent in radiation counting. The coefficient of variation (CV) for different time intervals was computed, with values below 5% in the first 200 s and increasing to approximately 10% for measurements beyond 600 s due to the lower counting rates. So, Figure 1 effectively demonstrates the expected behavior of radioactive decay, confirming the theoretical predictions for the elution of ^{137}Ba. The observed half-life of approximately 245 s aligns well with theoretical expectations. The obtained data validate the reliability of the experimental setup and highlight the importance of precise background radiation subtraction, particularly at lower activity levels.

Figure 2 illustrates the logarithm of the counting rate as a function of time, demonstrating the radioactive decay of the isotope ^{137}Ba.

At the beginning of the experiment ($t = 0$), the logarithm of the counting rate is approximately 3.8, corresponding to an initial activity of around 45 to 50 counts per second. Over the first 160 seconds, a significant decrease in activity is observed, with the logarithmic value dropping to approximately 3.0, indicating that the detected count rate has nearly halved within this timeframe. By 320 seconds, the logarithm of the counting rate has further decreased to around 2.4, while after 500 seconds, it approaches values close to 1.8, showing a gradual but steady decline in activity.

Beyond 600 seconds, the logarithm of the counting rate falls below 1.5, corresponding to a measured count rate of approximately 4 to 5 counts per second. As time progresses beyond 800 seconds, the values fluctuate significantly due to the statistical nature of radioactive decay and the reduced count rate nearing background radiation levels. Despite these variations, the general trend follows a linear decrease, supporting the theoretical exponential decay law.

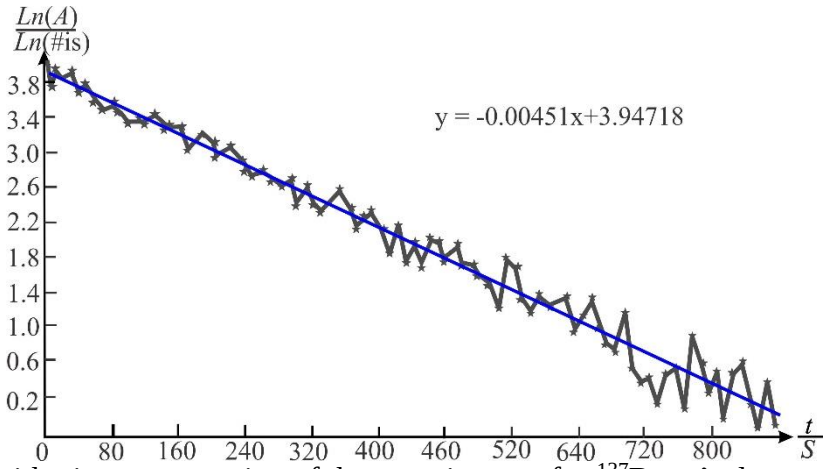

Figure 2 – Logarithmic representation of the counting rate for ^{137}Ba-m's decay over time, with a fitted regression line

The equation of the best-fit line is given as $y = -0.00451x+3.94718$, where the slope represents the decay constant. From this value, the half-life of ^{137}Ba was determined to be approximately 153.69 seconds. This result is consistent with theoretical expectations, confirming the accuracy of the experiment. The half-life value indicates that the radioactive activity of the isotope is reduced by 50% approximately every 154 seconds.

The linearity of the logarithmic plot verifies the fundamental principle of exponential radioactive decay, where the activity of a radioactive isotope decreases proportionally to its remaining amount over time. The consistency of the experimental data with the fitted regression model further validates the accuracy of the measurement process. Fluctuations in the data, especially at later time intervals, are a result of the random nature of radioactive decay, which follows a Poisson distribution. The standard deviation of the residuals between the experimental data and the fitted regression line was computed to assess the goodness-of-fit, with results confirming a strong correlation between measured values and the theoretical decay model. The coefficient of determination (R^2) was found to be close to 0.99, indicating a high level of agreement between the measured data and the expected decay trend.

The variation in counting rate as a function of time, demonstrating the approach to radioactive equilibrium is presented in Figure 3.

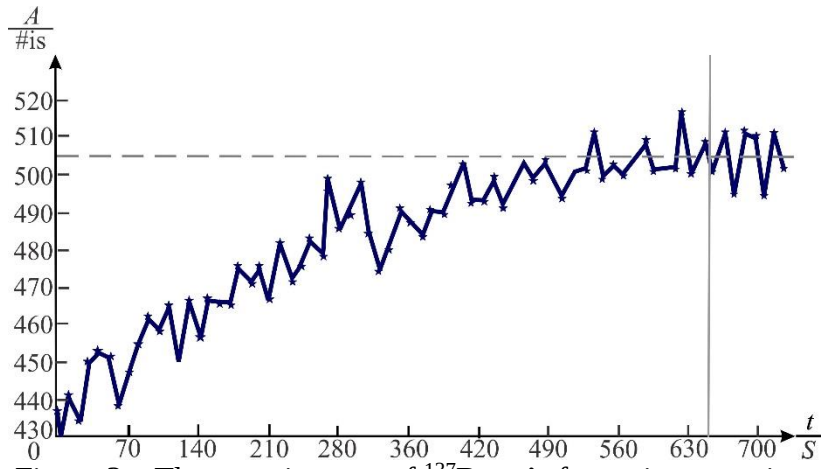

Figure 3 – The counting rate of ^{137}Ba-m's formation over time

The vertical axis represents the counting rate in counts per second, ranging from approximately 430 to 520, while the horizontal axis represents the elapsed time in seconds, covering a total duration of approximately 700 seconds. The experimental data points, marked along the curve,

indicate an increasing trend in activity over time, with fluctuations characteristic of statistical variations in radioactive decay measurements. A horizontal dashed line is included to represent the equilibrium activity level, while a vertical marker at approximately 650 seconds indicates the point at which equilibrium is reached.

At the beginning of the experiment, the counting rate is approximately 430 counts per second. Over the first 200 seconds, a gradual increase in activity is observed, reaching around 460 counts per second. As time progresses beyond 400 seconds, the counting rate continues to rise, fluctuating between 470 and 490 counts per second. Around 600 seconds, the activity stabilizes close to 500 counts per second, and by 650 seconds, equilibrium is reached, with the counting rate fluctuating around an average value of approximately 504.28 counts per second. Beyond 650 seconds, the fluctuations in activity become more pronounced but remain centered around the equilibrium value. The statistical nature of radioactive decay contributes to these variations, and the presence of background radiation and instrumental noise may also influence the recorded values. At equilibrium, the total counting rate comprises contributions from two components: the residual activity from the initial isotope (N_0) and the activity from the decay product ($\bar{N}$). By subtracting the equilibrium activity value from the actual measured counting rate, the contribution of the decaying isotope can be isolated. In this case, after reaching equilibrium at approximately 650 seconds, the recorded counting rate stabilizes at 504.28 counts per second, confirming that the system has reached a steady-state condition. The increasing trend in activity and subsequent stabilization at an equilibrium value align with theoretical expectations for radioactive decay processes where daughter isotopes contribute to overall activity. The presence of fluctuations in the data is consistent with Poisson noise, inherent to radiation counting. The CV was computed to quantify these fluctuations, and the results indicate a stable equilibrium state beyond 650 seconds.

Figure 4 presents the natural logarithm of the counting rate as a function of time, illustrating the decay behavior of the radioactive equilibrium activity.

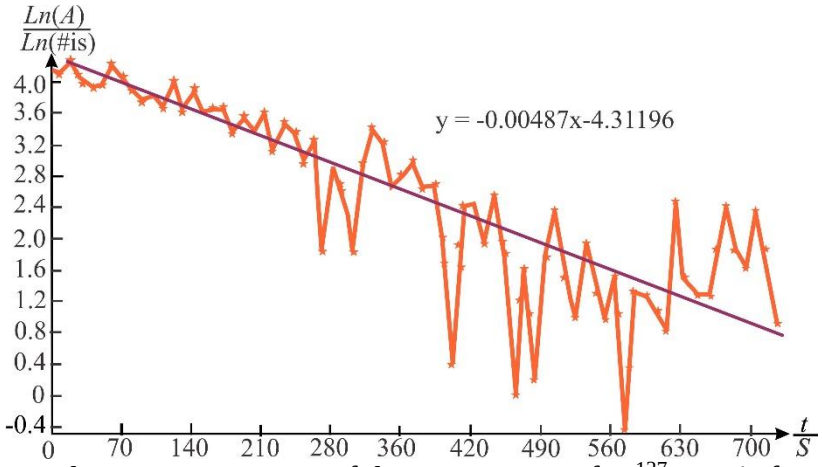

Figure 4 – The logarithmic representation of the counting rate for ^{137}Ba-m's formation over time, accompanied by a fitted regression line

The vertical axis represents the logarithmic activity values, ranging from approximately -0.4 to 4.0, while the horizontal axis represents the elapsed time in seconds, covering a total duration of approximately 700 seconds. The experimentally obtained data points are shown in orange, demonstrating a decreasing trend over time, with notable fluctuations at later stages. A fitted regression line, shown in purple, provides a mathematical representation of the decay trend.

At the beginning of the measurement (t = 0), the logarithm of the counting rate is approximately 4.0, corresponding to a high initial activity level. Over the first 200 seconds, a steady decline is observed, with the logarithmic value dropping to around 3.2. Between 300 and 500 seconds, the trend continues downward with moderate fluctuations, and by 600 seconds, the activity falls below 2.0. At later times, beyond 650 seconds, significant variations appear, likely due to statistical

fluctuations in radiation counting. Despite these variations, the overall trend follows a near-linear decrease, confirming the expected exponential decay behavior. The fitted regression line provides an analytical model for extracting key decay parameters, including the half-life of the isotope.

The regression equation for the logarithmic decay is given as: $y = -0.00487x - 4.31196$, where the slope of the line, -0.00487, represents the decay constant. The half-life is determined using the relationship between the decay constant and the natural logarithm of two. By applying this formula, the calculated half-life for this measurement is approximately 142.33 seconds. The logarithmic transformation of the decay data confirms the fundamental principle of exponential radioactive decay. The experimental half-life of 142.33 seconds is in agreement with literature values for the decay of the equilibrium activity. The deviations observed in later stages of the experiment can be attributed to statistical variations, detector sensitivity limitations, and environmental factors influencing the measurement process.

The consistency between the experimental data and the fitted regression line validates the accuracy of the measurement and confirms the applicability of the exponential decay model. The computed half-life closely aligns with theoretical expectations, further reinforcing the reliability of the experimental methodology.

4. Conclusions

1. The study successfully determined the half-life of the radioactive equilibrium activity, yielding a value of 142.33 s, which aligns with theoretical expectations. The decay constant was measured as 0.00487 s^{-1}, confirming the exponential nature of the process.

2. The logarithmic analysis of the counting rate demonstrated a linear relationship with time, validating the radioactive decay model. The counting rate stabilized at 504.28 counts per second after 650 s, confirming the establishment of equilibrium activity.

3. The observed data exhibited statistical fluctuations, particularly at lower activity levels, due to the inherent stochastic nature of radioactive decay. Despite these variations, the regression analysis confirmed a strong correlation with theoretical predictions.

4. The study effectively addressed the research problem by demonstrating the method for determining half-life using experimental decay data. The results confirmed the feasibility of measuring radioactive equilibrium and decay constants with high accuracy.

5. The primary constraint of the study was the presence of measurement noise and statistical deviations at later time intervals. Further research could focus on increasing data collection intervals, improving detector sensitivity, and minimizing external influences to enhance measurement precision.

References

[1] D. C. Kweon, J. Choi, K. R. Dong, W. K. Chung, H. J. Song, and Y. J. Kim, "Use of a GM counter to measure the half-life of Ba-137m generated by using an isotope generator," *J. Korean Phys. Soc.*, vol. 65, no. 4, pp. 532–540, Sep. 2014, doi: 10.3938/JKPS.65.532/METRICS.

[2] A. Miskiewicz and G. Zakrzewska-Trznadel, "Investigation of hydrodynamic behaviour of membranes using radiotracer techniques," *EPJ Web Conf.*, vol. 50, 2013, doi: 10.1051/EPJCONF/20135001005.

[3] H. Kasban, H. Arafa, and S. M. S. Elaraby, "Principle component analysis for radiotracer signal separation," *Appl. Radiat. Isot.*, vol. 112, pp. 20–26, Jun. 2016, doi: 10.1016/J.APRADISO.2016.03.005.

[4] H. Utsunomiya *et al.*, "γ -ray strength function for barium isotopes," *Phys. Rev. C*, vol. 100, no. 3, Sep. 2019, doi: 10.1103/PHYSREVC.100.034605.

[5] A. Vogt *et al.*, "Isomers and high-spin structures in the N=81 isotones Xe 135 and Ba 137," *Phys. Rev. C*, vol. 95, no. 2, Feb. 2017, doi: 10.1103/PHYSREVC.95.024316.

[6] L. Kaya *et al.*, "Identification of high-spin proton configurations in Ba 136 and Ba 137," *Phys. Rev. C*, vol. 99, no. 1, Jan. 2019, doi: 10.1103/PHYSREVC.99.014301.

[7] E. Altuntaş, J. Ammon, S. B. Cahn, and D. Demille, "Demonstration of a Sensitive Method to Measure Nuclear-Spin-Dependent Parity Violation," *Phys. Rev. Lett.*, vol. 120, no. 14, Apr. 2018, doi: 10.1103/PHYSREVLETT.120.142501.

[8] K. Moran *et al.*, "E5 decay from the Jπ=11/2- isomer in Ba 137," *Phys. Rev. C - Nucl. Phys.*, vol. 90, no. 4, Oct.

2014, doi: 10.1103/PHYSREVC.90.041303.
[9] Diana, "5. Radiation Measurements: Instruments And Methods Joint innovative training and teaching/ learning program in enhancing development and transfer knowledge of application of ionizing radiation in materials processing".
[10] V. Sivasailanathan, P. Kumar, and S. Sagadevan, "Calibration and estimation of efficiency of Geiger Muller counter using a standard radioactive source," *Int. J. Phys. Sci. Full Length Res. Pap.*, vol. 12, no. 1, pp. 8–12, 2017, doi: 10.5897/IJPS2016.4566.
[11] "Methods to identify and locate spent radiation sources".
[12] "Only One Earth: 4 Ways Nuclear Science is Helping the Environment | IAEA." Accessed: Mar. 10, 2025. [Online]. Available: https://www.iaea.org/newscenter/news/only-one-earth-4-ways-nuclear-science-is-helping-the-environment

Information about authors:
Milana Bushina – PhD Student, Research Engineer, Department of Nuclear Physics, Peter the Great St.Petersburg Polytechnic University, St. Petersburg, Russian Federation, milana.bushina@bk.ru

Author Contributions:
Milana Bushina – concept, methodology, resources, data collection, testing, modeling, analysis, visualization, interpretation, drafting, editing, funding acquisition.

Conflict of Interest: The authors declare no conflict of interest.

Use of Artificial Intelligence (AI): The authors declare that AI was not used.

Received: *31.01.2024*
Revised: 10.03.2025
Accepted: 12.03.2025
Published: 13.03.2025

Technobius Physics, 2025, 3(1), 0026, DOI: https://doi.org/10.54355/tbusphys/3.1.2025.0026

Technobius Physics

https://technobiusphysics.kz/

e-ISSN 3007-0147

Article

Synthesis and research of optical and electrical properties of tin dioxide nanoprolocs in the SiO_2/Si track template

Diana Junisbekova*, Zein Baimukhanov, Alma Dauletbekova

Faculty of Physics and Technical Sciences, L.N. Gumilyov Eurasian National University, Astana, Kazakhstan
*Correspondence: diana911115@gmail.com

Abstract. This work presents a study of the structural, optical and electrical characteristics of tin dioxide (SnO_2) nanowires obtained by chemical deposition (CD) into SiO2/Si track templating (templating synthesis). Latent tracks in the SiO2 layer were created by irradiation with fast heavy ions (FHE) Xe at 200 MeV energy with fluence F = 108 cm-2 followed by etching in 4% aqueous hydrofluoric acid (HF) solution. The selected XO method is widely used for the deposition of semiconductor oxide nanowires in SiO_2 nanopores. The CW method is cost-effective because it does not require any special equipment for the deposition of nanowires. To realize the deposition, a solution of metal coordination compound and reducing agent is used. To analyze the pore filling after CW process, the surface morphology of the samples was investigated using Zeiss Crossbeam 540 scanning microscope. The crystallographic structure of SnO2/SiO2/Si nanostructures with SnO_2 nanopore filling was investigated by X-ray diffraction. X-ray diffraction analysis (XRD) is performed on a Rigaku SmartLab X-ray diffractometer. A SnO_2-NP/SiO_2/Si nanostructure with orthorhombic crystalline structure of SnO_2 nanowires supplemented with metallic tin was obtained. The photoluminescence spectra were measured under excitation with 5.17 eV wavelength light using a CM2203 spectrofluorimeter. Gaussian decomposition of the photoluminescence spectra of SnO2-NP/SiO_2/Si structures, showed that they have low intensity, which is mainly due to the presence of defects such as oxygen vacancies, interdomain tin or tin with damaged bonds. The electrical characterization study was carried out using a VersaStat 3 patentiostat. The WAC measurement of the nanowire obtained by chemical deposition showed that due to the presence of metallic tin, the conductivity is close to metallic.
Keywords: SiO_2/Si track templating; chemical deposition; SnO_2 nanowires, tin dioxide; templating synthesis.

1. Introduction

With the manifestation of special properties of various nanoscale objects, a great interest in their research has arisen in recent years. Depending on the application, materials with different functional properties are selected. Today's technologies make it possible to control the morphology of such materials at the nanoscale in order to obtain a large variety of nanostructures (NS) with desired properties [1], [2], [3].

One of the simplest ways to form nanomaterials is the use of nanoporous templates (matrices) [4], [5], [6]. Using this method, different structures can be obtained due to the self-organization of materials of this class inside the pores. The use of pores allows to obtain nanoparticles, nanorods, nanofibers and nanowires from semiconductors [7], [8] metals [9], [10], [11] and others.

At present, with the introduction of silicon-based nanosystems in technological processes, the most advantageous is the use of templates based on silicon oxide. We can use templates with different pore parameters i.e. diameter, aspect ratio and numerical density as required.

A more economical method is silicon oxide templates (pore diameters ~ 100 nm), which is possible by using porous silicon [12] or direct sputtering of porous a-SiO_2 by plasma chemical vapor deposition [12], [13]. To date, the potential of this type of technique to create templates from porous

a-SiO2 layers on Si has already been extensively investigated [14], [15], [16], [17], [18], [19], [20], [21].

The pores in the SiO_2 layer are formed using track technology, which includes fast heavy ion irradiation (FHI) and chemical etching process [18], [22]. Next, the process of filling the nanopores with different materials is carried out. In our case, we consider the deposition of tin dioxide.

Tin (VI) oxide is a semiconducting oxide with n-type conductivity. Its unique electrical and optical properties make it a promising material. In addition, SnO_2 has a number of excellent properties such as low electrical resistance, high electrical conductivity and high optical transparency in the visible electromagnetic range, and such properties of this material offer opportunities to utilize them in the development of novel applications for nanodevices.

Compared with other semiconductors, SnO_2 is an important functional material which is widely used in transparent conductors [23], transistors [24], optoelectronic devices [25], [26] gas sensors [27], etc.

Today, the templating method [28], hydrothermal method [29], chemical vapor deposition (CVD) [30], [31] and electrochemical deposition [32] are used to synthesize SnO_2 nanostructures with different morphologies.

In our work, we chose the templating synthesis method to fill or produce tin dioxide (SnO_2) nanowires in SiO_2/Si track templates. This synthesis method is considered more economical to obtain such heterostructures ($SnO_2/SiO_2/Si$) with SnO_2 nanopore filling. Our chosen template synthesis is based on chemical and electrochemical deposition of materials into nanoporous substrates. An attractive aspect of template synthesis, is the possibility to tailor the physical, chemical and electronic properties of the nanomaterial by controlled manipulation of morphology, pore density, shape and size. The aim of the research conducted in this work is to form nanowires with orthorhombic crystal structure by controlling the resulting properties. Controlling the morphology of SnO_2 nanomaterials can improve their performance and expand their range of applications to create devices that solve new problems.

2. Methods

In the present work, the SiO_2/Si structure, (n - type) formed by thermal oxidation of silicon crystals in a humid oxygen atmosphere (900℃) was used. According to the data obtained by ellipsometry, the thickness of the oxide layer is 700 nm. To create discontinuous tracks in the SiO_2 matrix, the prepared samples were irradiated on a DC-60 gas pedal, with 132Xe ions with an energy of 200 MeV, the fluence value was in the range of 107 - 108 cm^{-2}.

A 4% aqueous solution of hydrofluoric acid (HF) with m(Pd)=0.025 g was used to form nanoporous templates in the samples irradiated with fast heavy ions (BTI). Etching was performed at room temperature for a certain time under a special fume hood. The size of the nanopores was adjusted depending on the etching time. After the treatment process in HF solution, the samples underwent a washing step in deionized water.

In the present work, chemical precipitation (CP) method was used to fill the nanopores. Chemical deposition is a widely used method for the deposition of semiconductor oxide nanowires (NWs) in SiO_2 nanopores. For deposition, a solution of a coordination compound of a metal and a reducing agent must be used. Unlike the electrochemical method, this method does not require an electrochemically conducting surface. The process starts with the deposition of material on the pore walls, resulting in the formation of a hollow tube inside each pore when the deposition time is short, and when the deposition time is long, solid nanowires are formed. This method does not require any special equipment and is considered low cost, all the components for the deposition of semiconductor oxide nanowires are dissolved in 100 ml of deionized water using magnetic stirrer at a certain time [33].

To obtain tin dioxide (SnO_2) nanowires using the CW method, a sulfate solution with the following composition was used: 0.67 g tin sulfate ($SnSO_4$) + 4 g thiourea (CH_4N_2S) + 2 mL sulfuric acid (H2SO4). CH_4N_2S was pre-dissolved in deionized water and SnSO4 was in turn dissolved in a

minimal volume of concentrated sulfuric acid (hh). The two solutions were then combined, and the pH value of the solution was adjusted in the range of values from 2 to 4 in order to optimize the conditions for the precipitation process. The CW process was carried out at a temperature of 323 K. The process was carried out under thorough mixing conditions using a LOIP LS-110 orbital shaker, to ensure uniform distribution of the reagents and to achieve the desired deposition density.

Detailed study of the obtained nanowires (nanostructures) and interpretation of the measurement results requires the use of modern developments in the field of measuring and diagnostic equipment. Scanning electron microscopy (SEM) and X-ray diffraction analysis (XRD) techniques are the main methods to investigate the structural features and surface morphologies of nanomaterials.

To analyze the pore-filled, as well as to investigate the structural features and surface morphology of SiO_2/Si track templates, after CW, the samples were examined using a Zeiss Crossbeam 540 dual-beam scanning microscope (SEM, Germany) at 2-5 kV equipped with a backscattered electron detector.

Using the X-ray diffraction analysis (XRD) technique, complete information on various properties as well as on the phase composition of the $SnO_2/SiO_2/Si$ structures was obtained. The PCA spectra were identified using a Rigaku SmartLab X-ray diffractometer equipped with a HyPix3000 high-energy 2D HPAD detector. Using TOPAS 4.2 software and the international ICDD database (PDF-2 Release 2020 RDB), standard phase composition determination and determination of crystal cell parameters based on the obtained diffractograms are carried out.

Luminescence spectra at room temperature in the spectral range of 300 to 800 nm with 240 nm excitation were recorded using a CM2203 spectrofluorimeter. The spectrofluorimeter provides highly sensitive measurements in the ultraviolet and visible spectral range. The use of two double monochromators provides a minimum level of interfering radiation, which guarantees high accuracy of measurements.

A VersaStat 3 potentiostat was used to investigate the electrical properties of the arrays of the obtained nanowires. This instrument supports maximum current up to ±2 A, voltage up to ±12 V. The volt-ampere characteristics were taken from an array of 0.7 cm2 filled nanochannels. The setup for measuring the VAC was assembled as follows: the sample was placed between two metal plates, to ensure that the plates cover only the part of the matrix that contains the nanowires. The plates were then connected to a power source by connecting a potentiostat in series. All VACs were performed using a 2nd order polynomial approximation [34].

3. Results and Discussion

Figure 1 shows the SEM pattern of the template surface after chemical deposition.

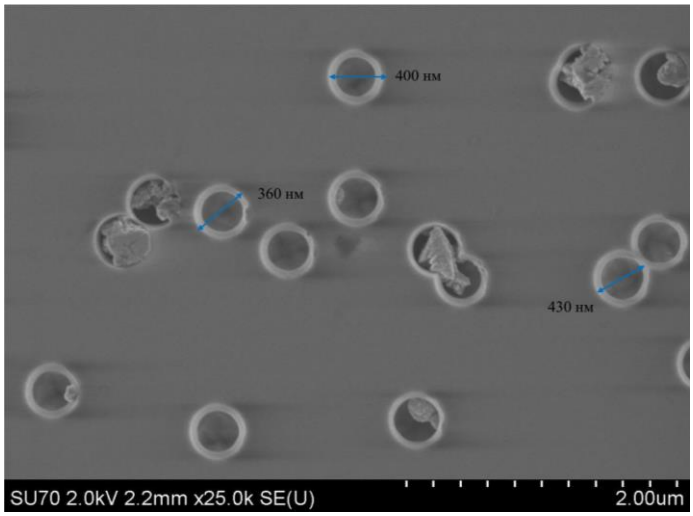

Figure 1 - SEM image of SiO2/Si-n template surface after SnO2 CW (tossing= 20 min, T = 323 K)

As can be seen in Figure 1, the filled nanochannels can be clearly seen when chemically deposited for 20 min. From the analysis of SEM images (Figure 2), we can see that the diameter of nanopores varies between 350 nm and 430 nm. The filling degree of the nanochannels is 80%.

According to the PCA data (Figure 2), chemical precipitation in sulfate solution in SiO_2/Si track templating led to the formation of SnO_2 nanowires with orthorhombic structure and spatial symmetry group Pnnm(58), also appeared Sn phase with tetragonal structure and spatial symmetry group I4/mmm (139).

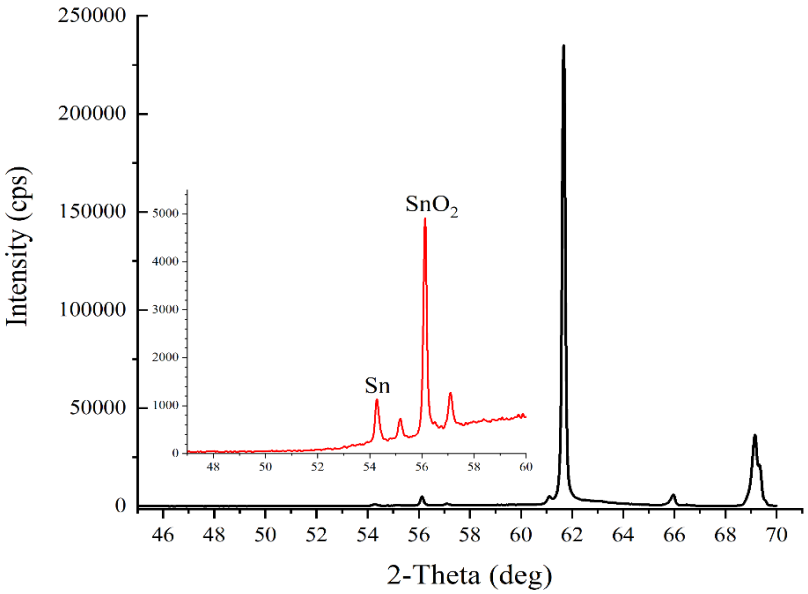

Figure 2 - X-ray diffractogram of SnO_2 samples obtained by CW method for 20 minutes

The results of X-ray diffraction analysis for this sample are shown in Table 1.

Table 1 – Crystallographic parameters of SnO_2 nanowires in SiO_2/Si-n track templated SiO_2/Si-n by PCA results

Phase name	Sn	SnO_2
Type of structure	Tetragonal	Orthorhombic
Prostrate group	139: I4/mmm	58: Pnnm
(hkl)	(002)	(220)
2θ	54.271	56.113
d, Å	1.6889	1.6377
L, nm	648	637
FWHM	0.144	0.15
Lattice parameters, Å	a(A) = 3.674736;	a(A) = 4.655800;
Volume, Å3	b(A) = 3.674736;	b(A) = 4.599800;
Crystallite size, $Å^3$	c(A) = 3.377628	c(A) = 3.151400
Density, g/cm^3	45.610417	67.489592

According to the results of X-ray diffraction analysis, we can conclude that the concentration ratio of Sn phase to SnO_2 phase is 22% by 78%, respectively.

The cell parameters obtained in experimental [35], [36] and theoretical works [37] are in good agreement with the data obtained for our orthorhombic tin dioxide nanowires.

Optical investigation techniques such as photoluminescence (PL) were used to determine the defects and impurities in the obtained nanowires. The photoluminescence (PL) of SnO_2-NP/SiO_2/Si nanostructure was investigated in the spectral range of 2 - 3.2 eV when excited by light with wavelength λ = 5.17 eV. Figure 3 shows the Gaussian decomposition of the photoluminescence spectrum of SnO_2-NP/SiO_2/Si structures obtained by chemical deposition. SiO_2 luminescence is taken into account in the photoluminescence spectrum.

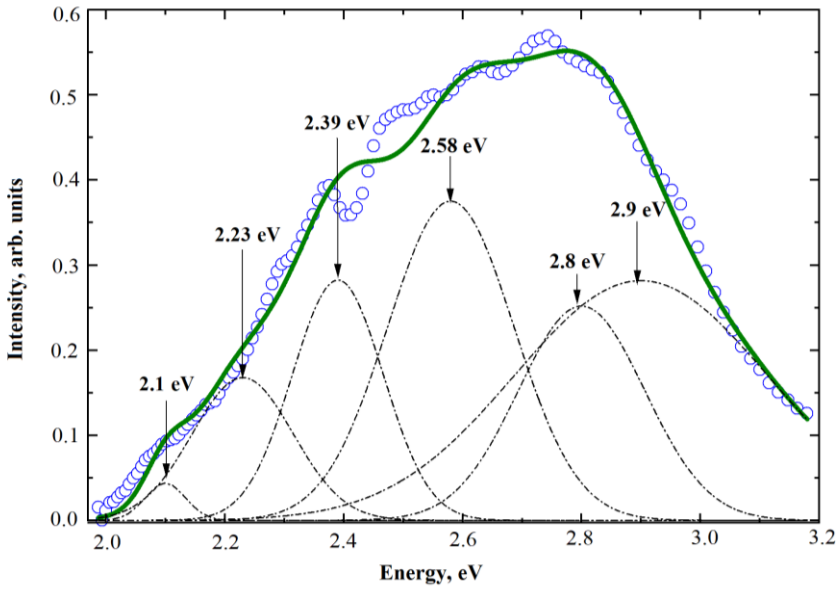

Figure 3 – Gaussian decomposition of the photoluminescence spectrum of SnO_2-NP/SiO_2/Si structures

The PL spectra of nanowires obtained by chemical deposition show differences compared to the PL spectra of nanowires synthesized by electrochemical method, characterized by higher intensity maxima. Impurities and defects present in the material due to different synthesis method, solutions used and temperature may play a key role in the variation of the intensity of the PL spectra. The observed intense peaks at 2.9 eV, 2.8 eV, 2.58 eV, 2.39 eV, 2.23 eV, 2.1 eV on the luminescence spectrum agree well with the results of similar measurements by researchers [38]. It is widely known from the authors [39], the emission of visible light is related to the energy levels of defects in the forbidden band of SnO2 associated with O-vacancies and Sn interstitials. The luminescence centers responsible for the violet emission maximum at 2.9 eV can be attributed to interstitial tin or tin with damaged bonds [40], [41], [42], [43], [44]. The blue light emission with a maximum at 2.8 eV can be due to the transition from the triplet state to the ground state for V_O^0 [45]. Most of the oxygen vacancies are in the paramagnetic state of V_O^+ with a peak at 2.58 eV [46], [42] and the peak at 2.39 eV [47] corresponds to the surface donor V_O^0. The 2.23 eV peak is probably the result of oxygen vacancies that are formed during the deposition process as indicated by [48], [49]. The maximum at 2.1 eV is related to defect levels in the forbidden band associated with O vacancies or interstitial Sn, which was observed in the case of SnO2 nanoribbons synthesized by laser ablation [50] and SnO_2 nanorods that were obtained by growth from solution phase [51]. It is widely known that oxygen vacancies are the most frequent type of defects and often act as emitting defects in the occurrence of luminescence. Indeed, the analysis of the FL spectrum shows that it is oxygen vacancies rather than tin-related defects that are the main defects.

The study of the voltammetric characteristic of the SnO_2-NP/SiO_2/Si structure allows us to determine the type of conductivity of the synthesized structure. The voltammetric characteristic (VAC) was measured from an array of filled nanochannels with an area of 0.7 cm². Figure 4 presents the VAC of the samples before and after deposition, demonstrating the influence of the synthesis process on the electrical properties of the structure.

The obtained VAC exhibits a nonlinear, asymmetric shape, indicating a deviation from ideal ohmic behavior. This suggests the presence of a Schottky barrier or other charge transport mechanisms influenced by the material's defect structure and metallic inclusions.

The curve shows an increase in conductivity after deposition, which can be attributed to the incorporation of metallic tin, leading to enhanced charge carrier mobility. In the negative voltage region, a pronounced increase in current is observed, further supporting the presence of metallic conductivity components.

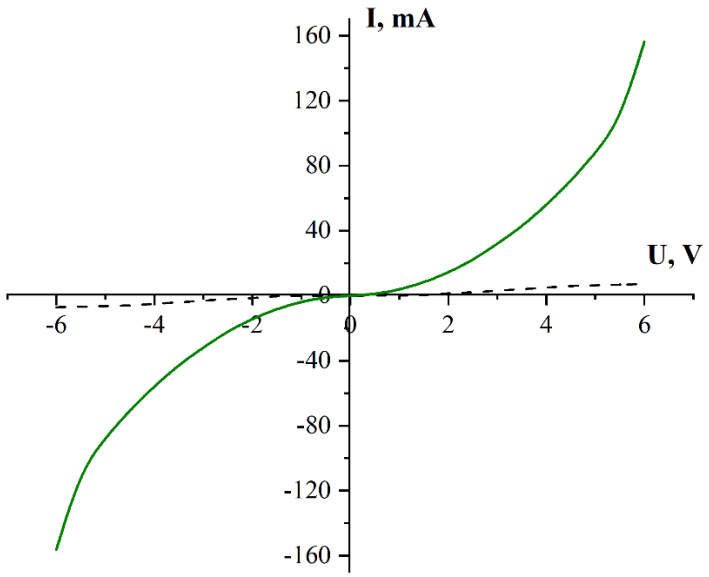

Figure 4 – Volt-ampere characteristic of SnO_2-NP/SiO_2/Si: dotted curve - original sample; solid curve - with deposited SnO_2 (tossing= 20 min, T = 323 K)

Overall, the results highlight the impact of structural modifications on the electronic properties of the SnO_2-NP/SiO_2/Si system, emphasizing the role of metallic tin in altering the charge transport mechanism.

4. Conclusions

In this study, tin dioxide (SnO_2) nanowires were synthesized by chemical deposition into SiO_2/Si track templates. X-ray structural analysis confirmed that the obtained nanowires exhibit an orthorhombic crystal structure with lattice parameters: a = 4.655800 Å, b = 4.599800 Å, c = 3.151400 Å. Additionally, the presence of metallic tin was detected, which significantly influences their physicochemical properties.

Photoluminescence spectrum analysis revealed a broad emission band in the energy range from 2 eV to 3.2 eV, indicating the complex nature of radiative processes. Investigation of the defect structure showed that the dominant point defects are oxygen vacancies, which play a key role in shaping the optical properties of the material. Moreover, spectral maxima associated with interdomain tin atoms and tin with broken chemical bonds were identified. These defects can act as effective recombination centers and influence the mechanisms of charge carrier generation and relaxation.

Analysis of the current-voltage characteristics (I-V curves) of SnO_2 nanowires with an orthorhombic crystal structure demonstrated that, due to the presence of metallic tin, their conductivity approaches a metallic type. This indicates a significant modification of the electronic structure compared to pure tin dioxide, which typically exhibits semiconductor properties. The presence of metallic inclusions may contribute to the formation of tunneling junctions and localized conductive channels, making such nanostructures promising for applications in nanoelectronics, sensing, and hybrid electronic devices.

Thus, the obtained results demonstrate the possibility of precisely controlling the structural, optical, and electrical properties of SnO_2 nanowires through the incorporation of metallic tin, opening new prospects for their practical applications.

References

[1] D. V. Talapin, J. S. Lee, M. V. Kovalenko, and E. V. Shevchenko, “Prospects of colloidal nanocrystals for electronic and optoelectronic applications,” *Chem. Rev.*, vol. 110, no. 1, pp. 389–458, Jan. 2010, doi: 10.1021/CR900137K/ASSET/IMAGES/CR-2009-00137K_M028.GIF.

[2] “(PDF) Nanotechnology, Big things from a Tiny World: a Review.” Accessed: Mar. 13, 2025. [Online]. Available:

https://www.researchgate.net/publication/46189710_Nanotechnology_Big_things_from_a_Tiny_World_a_Review
[3] W. Lu and C. M. Lieber, "Nanoelectronics from the bottom up," *Nat. Mater. 2007 611*, vol. 6, no. 11, pp. 841–850, 2007, doi: 10.1038/nmat2028.
[4] M. R. Jones, K. D. Osberg, R. J. MacFarlane, M. R. Langille, and C. A. Mirkin, "Templated techniques for the synthesis and assembly of plasmonic nanostructures," *Chem. Rev.*, vol. 111, no. 6, pp. 3736–3827, Jun. 2011, doi: 10.1021/CR1004452/ASSET/CR1004452.FP.PNG_V03.
[5] D. Routkevitch, T. Bigioni, M. Moskovits, and J. M. Xu, "Electrochemical Fabrication of CdS Nanowire Arrays in Porous Anodic Aluminum Oxide Templates," *J. Phys. Chem.*, vol. 100, no. 33, pp. 14037–14047, Aug. 1996, doi: 10.1021/JP952910M.
[6] F. Zhang and D. Zhao, "Fabrication of ordered magnetite-doped rare earth fluoride nanotube arrays by nanocrystal self-assembly," *Nano Res.*, vol. 2, no. 4, pp. 292–305, Apr. 2009, doi: 10.1007/S12274-009-9027-6/METRICS.
[7] "Preparation of CdS Single-Crystal Nanowires by Electrochemically Induced Deposition - Xu - 2000 - Advanced Materials - Wiley Online Library." Accessed: Mar. 13, 2025. [Online]. Available: https://advanced.onlinelibrary.wiley.com/doi/10.1002/%28SICI%291521-4095%28200004%2912%3A7%3C520%3A%3AAID-ADMA520%3E3.0.CO%3B2-%23
[8] C. R. Martin, "Nanomaterials: A Membrane-Based Synthetic Approach," *Science (80-.).*, vol. 266, no. 5193, pp. 1961–1966, Dec. 1994, doi: 10.1126/SCIENCE.266.5193.1961.
[9] I. U. Schuchert, M. E. T. Molares, D. Dobrev, J. Vetter, R. Neumann, and M. Martin, "Electrochemical Copper Deposition in Etched Ion Track Membranes : Experimental Results and a Qualitative Kinetic Model," *J. Electrochem. Soc.*, vol. 150, no. 4, p. C189, Feb. 2003, doi: 10.1149/1.1554722.
[10] S. E. Demyanov *et al.*, "On the morphology of Si/SiO2/Ni nanostructures with swift heavy ion tracks in silicon oxide," *J. Surf. Investig.*, vol. 8, no. 4, pp. 805–813, Aug. 2014, doi: 10.1134/S1027451014040326/METRICS.
[11] V. Sivakov *et al.*, "Silver nanostructures formation in porous Si/SiO2 matrix," *J. Cryst. Growth*, vol. 400, pp. 21–26, Aug. 2014, doi: 10.1016/J.JCRYSGRO.2014.04.024.
[12] A. Barranco, J. Cotrino, F. Yubero, J. P. Espinós, and A. R. González-Elipe, "Room temperature synthesis of porous SiO2 thin films by plasma enhanced chemical vapor deposition," *J. Vac. Sci. Technol. A*, vol. 22, no. 4, pp. 1275–1284, Jul. 2004, doi: 10.1116/1.1761072.
[13] G. Amato, S. Borini, A. M. Rossi, L. Boarino, and M. Rocchia, "Si/SiO2 nanocomposite by CVD infiltration of porous SiO2," *Phys. status solidi*, vol. 202, no. 8, pp. 1529–1532, Jun. 2005, doi: 10.1002/PSSA.200461172.
[14] D. Fink, A. Chandra, P. Alegaonkar, A. Berdinsky, A. Petrov, and D. Sinha, "Nanoclusters and nanotubes for swift ion track technology," *Radiat. Eff. Defects Solids*, vol. 162, no. 3–4, pp. 151–156, Mar. 2007, doi: 10.1080/10420150601132487.
[15] Y. A. Ivanova *et al.*, "Electrochemical deposition of Ni and Cu onto monocrystalline n-Si(100) wafers and into nanopores in Si/SiO2 template," *J. Mater. Sci.*, vol. 42, no. 22, pp. 9163–9169, Nov. 2007, doi: 10.1007/S10853-007-1926-X/METRICS.
[16] K. Hoppe *et al.*, "An ion track based approach to nano- and micro-electronics," *Nucl. Instruments Methods Phys. Res. Sect. B Beam Interact. with Mater. Atoms*, vol. 266, no. 8, pp. 1642–1646, Apr. 2008, doi: 10.1016/J.NIMB.2007.12.069.
[17] A. Razpet, A. Johansson, G. Possnert, M. Skupiński, K. Hjort, and A. Hallén, "Fabrication of high-density ordered nanoarrays in silicon dioxide by MeV ion track lithography," *J. Appl. Phys.*, vol. 97, no. 4, Feb. 2005, doi: 10.1063/1.1850617/914557.
[18] A. Dallanora *et al.*, "Nanoporous SiO2/Si thin layers produced by ion track etching: Dependence on the ion energy and criterion for etchability," *J. Appl. Phys.*, vol. 104, no. 2, Jul. 2008, doi: 10.1063/1.2957052/936055.
[19] "Characteristic features of electric charge transfer processes in Si/SiO2/Ni nanostructures in strong magnetic fields | Request PDF." Accessed: Mar. 13, 2025. [Online]. Available: https://www.researchgate.net/publication/290999855_Characteristic_features_of_electric_charge_transfer_processes_in_SiSiO2Ni_nanostructures_in_strong_magnetic_fields
[20] L. A. Vlasukova *et al.*, "Threshold and criterion for ion track etching in SiO2 layers grown on Si," *Vacuum*, vol. 105, pp. 107–110, Jul. 2014, doi: 10.1016/J.VACUUM.2014.01.005.
[21] A. Benyagoub and M. Toulemonde, "Ion tracks in amorphous silica," *J. Mater. Res.*, vol. 30, no. 9, pp. 1529–1543, Jan. 2015, doi: 10.1557/JMR.2015.75/METRICS.
[22] E. Kaniukov, V. Bundyukova, M. Kutuzau, and D. Yakimchuk, "Peculiarities of formation and characterization of SiO2/Si ion-track template," *NATO Sci. Peace Secur. Ser. B Phys. Biophys.*, pp. 41–57, 2019, doi: 10.1007/978-94-024-1687-9_3.
[23] A. Vaseashta and D. Dimova-Malinovska, "Nanostructured and nanoscale devices, sensors and detectors," *Sci. Technol. Adv. Mater.*, vol. 6, no. 3-4 SPEC. ISS., pp. 312–318, Apr. 2005, doi: 10.1016/J.STAM.2005.02.018.
[24] J. C. Chou and Y. F. Wang, "Preparation and study on the drift and hysteresis properties of the tin oxide gate ISFET by the sol–gel method," *Sensors Actuators B Chem.*, vol. 86, no. 1, pp. 58–62, Aug. 2002, doi: 10.1016/S0925-4005(02)00147-8.
[25] J. S. Lee, S. K. Sim, B. Min, K. Cho, S. W. Kim, and S. Kim, "Structural and optoelectronic properties of SnO2 nanowires synthesized from ball-milled SnO2 powders," *J. Cryst. Growth*, vol. 267, no. 1–2, pp. 145–149, Jun. 2004, doi: 10.1016/J.JCRYSGRO.2004.03.030.

[26] Z. Ying, Q. Wan, Z. T. Song, and S. L. Feng, "Controlled synthesis of branched SnO2 nanowhiskers," *Mater. Lett.*, vol. 59, no. 13, pp. 1670–1672, Jun. 2005, doi: 10.1016/J.MATLET.2005.01.044.
[27] Y. Fan, J. Liu, H. Lu, P. Huang, and D. Xu, "Hierarchical structure SnO2 supported Pt nanoparticles as enhanced electrocatalyst for methanol oxidation," *Electrochim. Acta*, vol. 76, pp. 475–479, Aug. 2012, doi: 10.1016/J.ELECTACTA.2012.05.067.
[28] H. Zhang *et al.*, "Preparation of SnO2 Nanowires by Solvent-Free Method Using Mesoporous Silica Template and Their Gas Sensitive Properties," *J. Nanosci. Nanotechnol.*, vol. 11, no. 12, pp. 11114–11118, 2011, doi: 10.1166/JNN.2011.3978.
[29] H. Zhang, Q. He, X. Zhu, D. Pan, X. Deng, and Z. Jiao, "Surfactant-free solution phase synthesis of monodispersed SnO2 hierarchical nanostructures and gas sensing properties," *CrystEngComm*, vol. 14, no. 9, pp. 3169–3176, Apr. 2012, doi: 10.1039/C2CE06558D.
[30] L. Yu, L. Zhang, H. Song, X. Jiang, and Y. Lv, "Hierarchical SnO2 architectures: controllable growth on graphene by atmospheric pressure chemical vapour deposition and application in cataluminescence gas sensor," *CrystEngComm*, vol. 16, no. 16, pp. 3331–3340, Mar. 2014, doi: 10.1039/C3CE42538J.
[31] H. Huang, O. K. Tan, Y. C. Lee, T. D. Tran, M. S. Tse, and X. Yao, "Semiconductor gas sensor based on tin oxide nanorods prepared by plasma-enhanced chemical vapor deposition with postplasma treatment," *Appl. Phys. Lett.*, vol. 87, no. 16, pp. 1–3, Oct. 2005, doi: 10.1063/1.2106006/910140.
[32] J. Pan *et al.*, "SnO2-TiO2 Core-shell nanowire structures: Investigations on solid state reactivity and photocatalytic behavior," *J. Phys. Chem. C*, vol. 115, no. 35, pp. 17265–17269, Sep. 2011, doi: 10.1021/JP201901B/ASSET/IMAGES/MEDIUM/JP-2011-01901B_0009.GIF.
[33] A. K. Dauletbekova, A. Y. Alzhanova, A. T. Akilbekov, A. A. Mashentseva, M. V. Zdorovets, and K. N. Balabekov, "Synthesis of Si/SiO2/ZnO nanoporous materials using chemical and electrochemical deposition techniques," *AIP Conf. Proc.*, vol. 1767, no. 1, Sep. 2016, doi: 10.1063/1.4962589/755185.
[34] A. Dauletbekova *et al.*, "Ion-Track Template Synthesis and Characterization of ZnSeO3 Nanocrystals," *Cryst. 2022, Vol. 12, Page 817*, vol. 12, no. 6, p. 817, Jun. 2022, doi: 10.3390/CRYST12060817.
[35] J. Haines and J. Léger, "X-ray diffraction study of the phase transitions and structural evolution of tin dioxide at high pressure:ffRelationships between structure types and implications for other rutile-type dioxides," *Phys. Rev. B*, vol. 55, no. 17, p. 11144, May 1997, doi: 10.1103/PhysRevB.55.11144.
[36] S. R. Shieh, A. Kubo, T. S. Duffy, V. B. Prakapenka, and G. Shen, "High-pressure phases in SnO2 to 117 GPa," *Phys. Rev. B - Condens. Matter Mater. Phys.*, vol. 73, no. 1, p. 014105, Jan. 2006, doi: 10.1103/PHYSREVB.73.014105/FIGURES/6/THUMBNAIL.
[37] L. Gracia, A. Beltrán, and J. Andrés, "Characterization of the High-Pressure Structures and Phase Transformations in SnO2. A Density Functional Theory Study," *J. Phys. Chem. B*, vol. 111, no. 23, pp. 6479–6485, Jun. 2007, doi: 10.1021/JP067443V.
[38] B. Wang and P. Xu, "Growth mechanism and photoluminescence of the SnO2 nanotwists on thin film and the SnO2 short nanowires on nanorods," *Chinese Phys. B*, vol. 18, no. 1, p. 324, Jan. 2009, doi: 10.1088/1674-1056/18/1/053.
[39] E. J. H. Lee, C. Ribeiro, T. R. Giraldi, E. Longo, E. R. Leite, and J. A. Varela, "Photoluminescence in quantum-confined SnO2 nanocrystals: Evidence of free exciton decay," *Appl. Phys. Lett.*, vol. 84, no. 10, pp. 1745–1747, Mar. 2004, doi: 10.1063/1.1655693.
[40] S. Munnix and M. Schmeits, "Electronic structure of tin dioxide surfaces," *Phys. Rev. B*, vol. 27, no. 12, p. 7624, Jun. 1983, doi: 10.1103/PhysRevB.27.7624.
[41] N. Chiodini, A. Paleari, D. Dimartino, and G. Spinolo, "SnO2 nanocrystals in SiO2: A wide-band-gap quantum-dot system," *Appl. Phys. Lett.*, vol. 81, no. 9, pp. 1702–1704, Aug. 2002, doi: 10.1063/1.1503154.
[42] K. Vanheusden, W. L. Warren, C. H. Seager, D. R. Tallant, J. A. Voigt, and B. E. Gnade, "Mechanisms behind green photoluminescence in ZnO phosphor powders," *J. Appl. Phys.*, vol. 79, no. 10, pp. 7983–7990, May 1996, doi: 10.1063/1.362349.
[43] Y. Liu, Q. Yang, and C. Xu, "Single-narrow-band red upconversion fluorescence of ZnO nanocrystals codoped with Er and Yb and its achieving mechanism," *J. Appl. Phys.*, vol. 104, no. 6, Sep. 2008, doi: 10.1063/1.2980326/343684.
[44] K. G. Godinho, A. Walsh, and G. W. Watson, "Energetic and Electronic Structure Analysis of Intrinsic Defects in SnO2," *J. Phys. Chem. C*, vol. 113, no. 1, pp. 439–448, Jan. 2008, doi: 10.1021/JP807753T.
[45] Y. C. Her, J. Y. Wu, Y. R. Lin, and S. Y. Tsai, "Low-temperature growth and blue luminescence of SnO2 nanoblades," *Appl. Phys. Lett.*, vol. 89, no. 4, Jul. 2006, doi: 10.1063/1.2235925/986618.
[46] S. Rani, S. C. Roy, N. Karar, and M. C. Bhatnagar, "Structure, microstructure and photoluminescence properties of Fe doped SnO2 thin films," *Solid State Commun.*, vol. 141, no. 4, pp. 214–218, Jan. 2007, doi: 10.1016/J.SSC.2006.10.036.
[47] M. Bhatnagar, V. Kaushik, A. Kaushal, M. Singh, and B. R. Mehta, "Structural and photoluminescence properties of tin oxide and tin oxide: C core-shell and alloy nanoparticles synthesised using gas phase technique," *AIP Adv.*, vol. 6, no. 9, p. 95321, Sep. 2016, doi: 10.1063/1.4964313/884807.
[48] J. Duan *et al.*, "Multiform structures of SnO2 nanobelts," *Nanotechnology*, vol. 18, no. 5, p. 055607, Jan. 2007, doi: 10.1088/0957-4484/18/5/055607.
[49] L. Zhang, S. Ge, Y. Zuo, B. Zhang, and L. Xi, "Influence of oxygen flow rate on the morphology and magnetism of SnO 2 nanostructures," *J. Phys. Chem. C*, vol. 114, no. 17, pp. 7541–7547, May 2010, doi:

10.1021/JP9065604/ASSET/IMAGES/MEDIUM/JP-2009-065604_0007.GIF.
[50] J. Hu, Y. Bando, Q. Liu, and D. Golberg, "Laser-Ablation Growth and Optical Properties of Wide and Long Single-Crystal SnO2 Ribbons," *Adv. Funct. Mater.*, vol. 13, no. 6, pp. 493–496, Jun. 2003, doi: 10.1002/ADFM.200304327.
[51] B. Cheng, J. M. Russell, W. Shi, L. Zhang, and E. T. Samulski, "Large-Scale, Solution-Phase Growth of Single-Crystalline SnO2 Nanorods," *J. Am. Chem. Soc.*, vol. 126, no. 19, pp. 5972–5973, May 2004, doi: 10.1021/JA0493244/SUPPL_FILE/JA0493244SI20040402_033424.PDF.

Information about authors:
Diana Junisbekova – Doctor PhD, Senior Lecturer, Faculty of Physics and Technical Sciences, L.N. Gumilyov Eurasian National University, Astana, Kazakhstan, diana911115@gmail.com
Zein Baimukhanov – Candidate of Physical and Mathematical Sciences, Acting Associate Professor, Faculty of Physics and Technical Sciences, L.N. Gumilyov Eurasian National University, Astana, Kazakhstan, baimukhanov_zk@enu.kz
Alma Dauletbekova – Doctor of Physical and Mathematical Sciences, Professor, Faculty of Physics and Technical Sciences, L.N. Gumilyov Eurasian National University, Astana, Kazakhstan, dauletbekova_ak@enu.kz

Author Contributions:
Diana Junisbekova – data collection, testing, modeling, analysis, visualization.
Zein Baimukhanov – interpretation, drafting, editing, funding acquisition.
Alma Dauletbekova – concept, methodology, resources.

Conflict of Interest: The authors declare no conflict of interest.

Use of Artificial Intelligence (AI): The authors declare that AI was not used.

Received: *03.02.2025*
Revised: 26.02.2025
Accepted: 17.03.2025
Published: 18.03.2025

Technobius Physics, 2025, 3(1), 0027, DOI: https://doi.org/10.54355/tbusphys/3.1.2025.0027

Technobius Physics

https://technobiusphysics.kz/

e-ISSN 3007-0147

Article

Relaxation time measurement in liquids using compact NMR

Aigul Akkulova*

The computational materials science laboratory, National Laboratory Astana, Astana, Kazakhstan

*Correspondence: aigul.akkulova@mail.ru

Abstract. This study investigates the influence of experimental parameters on the accurate determination of longitudinal and transverse relaxation times in liquids using compact nuclear magnetic resonance relaxometry. Water and glycerin were selected as representative samples due to their contrasting viscosities and relaxation behaviors. The primary objective was to evaluate how repetition time, echo time, number of data points, and time step affect the precision of T_1 and T_2 measurements. Longitudinal relaxation times were determined using a variable repetition time method, while transverse relaxation times were measured via a multi-echo spin sequence. Exponential fitting algorithms were employed to extract relaxation parameters from recorded signal amplitudes. For water, the relaxation times were found to be approximately 3.0 s for T_1 and 1.423 s for T_2. In contrast, glycerin exhibited significantly shorter relaxation times, with T_1 estimated at 0.126 s and T_2 at 0.094 s. The results demonstrated that accurate estimation of relaxation times requires carefully optimized acquisition settings. Specifically, repetition time must exceed three times the T_1 value to ensure full longitudinal recovery, while short echo times and a high number of echoes are essential for reliable T_2 determination. The findings address a critical methodological gap in relaxometry protocols and offer practical recommendations for enhancing measurement accuracy in simple liquids.

Keywords: NMR relaxometry, longitudinal relaxation, transverse relaxation, spin echo, signal fitting.

1. Introduction

Nuclear magnetic resonance (NMR) relaxometry is a non-invasive and highly sensitive technique for probing the molecular dynamics and physical properties of liquids and soft matter. Two key parameters derived from NMR relaxometry are the longitudinal relaxation time (T_1) and the transverse relaxation time (T_2), which characterize the return of nuclear magnetization to equilibrium along and perpendicular to the external magnetic field, respectively. These relaxation times are fundamental to understanding spin–lattice and spin–spin interactions and are widely used in materials science, biophysics, and medical diagnostics [1], [2]. Accurate determination of T_1 and T_2 is essential for quantitative interpretation of NMR signals, optimization of imaging protocols, and the development of contrast agents.

Despite its broad applicability, the accuracy of relaxation time measurements is strongly dependent on the choice of experimental parameters such as repetition time (*TR*), echo time (TE), time resolution, and the number of data points. In practical settings, inappropriate selection of these parameters may lead to significant errors in estimated relaxation times, especially in samples with short T_1 or T_2 values [3]. This challenge is particularly relevant when studying complex fluids such as glycerin, where high viscosity leads to rapid signal decay and requires careful calibration of measurement sequences.

Recent research has addressed some of these challenges through methodological improvements in data acquisition and signal processing. For example, researchers developed a modified inversion-recovery sequence for more accurate T_1 estimation in viscous samples, emphasizing the importance of adjusting TR according to sample properties [4]. Similarly, authors implemented a multi-echo spin-echo protocol with adaptive echo spacing to improve T_2

measurements in tissue-mimicking phantoms [5]. In another study, the research team examined the effects of RF pulse miscalibration on exponential fitting models, showing that deviations from ideal 90° pulses distort relaxation curves [6]. Although these studies have advanced the precision of relaxometry techniques, they often assume either long T_1 times or homogeneous sample behavior, which limits their applicability to fast-relaxing, heterogeneous liquids such as glycerin or water in confined environments.

A critical limitation in previous studies is the insufficient evaluation of how experimental design — especially the interplay between TR, TE, and signal sampling — affects the accuracy of T_1 and T_2 determination in common liquids with contrasting physical properties. Furthermore, few works have presented direct side-by-side comparisons of relaxation behavior in substances with markedly different viscosities using compact NMR instruments.

Based on this research gap, we hypothesize that accurate estimation of T_1 and T_2 in liquids such as water and glycerin depends not only on sample properties but also critically on the optimization of timing and acquisition parameters in compact NMR systems. We further assume that both over- and underestimation of relaxation times can occur if the measurement protocol is not specifically tailored to the sample's relaxation characteristics.

The aim of this study is to systematically investigate the influence of experimental parameters — such as repetition time, echo time, number of echoes, and time step — on the accurate determination of T_1 and T_2 relaxation times in water and glycerin using a compact magnetic resonance tomograph. The study offers practical recommendations for protocol optimization and contributes to the broader understanding of how acquisition design affects the reliability of NMR relaxometry in simple liquids. The novelty of this work lies in the direct comparative analysis of two contrasting fluids under identical measurement conditions and the integration of exponential fitting with statistical validation to quantify relaxation behavior.

2. Methods

Magnetic resonance relaxation measurements were conducted using a compact NMR tomograph (Spin-Tech Company, USA). A 10 mm thick water sample was initially placed in the sample chamber of the device. The TR between two 90° radiofrequency (RF) pulses was varied to assess signal behavior. The measurement protocol began with a high TR value (e.g., 15 s), and the signal amplitude was recorded. Subsequently, the TR was incrementally reduced until the signal amplitude decreased by approximately 50%, indicating that the spin-lattice system had not fully relaxed between pulses. This procedure enabled estimation of the longitudinal relaxation time (T_1), as the TR corresponding to half signal intensity approximates the T_1 half-recovery point [7].

The calculated relaxation time was then used to configure the device parameters for exponential signal curve acquisition. The water sample was replaced with a 10 mm thick glycerin sample, and the same procedure was repeated. All control sliders were adjusted to ensure a clear exponential relaxation curve on the display. The selected repetition time was set to at least three times the computed T_1 value to ensure full magnetization recovery between pulses. The time step and number of data points were optimized so that the total effective measurement time between two 90° pulses covered a sufficient range, with finer time steps and more data points enhancing result reliability [8].

To further evaluate the transverse relaxation characteristics, spin-echo sequences were applied. Approximately 250 echo signals were recorded with an echo time (TE) of about 2 ms, producing a well-defined exponential decay curve. Echo times longer than necessary led to artificial dephasing effects due to the measurement sequence, resulting in underestimated relaxation times. Therefore, the TE was minimized to reduce such distortions. The recorded signal decay curves were fitted using an exponential regression model [9].

Finally, the glycerin sample was replaced with the initial 10 mm water sample, and the full measurement procedure was repeated. To examine the influence of the number of echoes and echo

time on curve fidelity, the number of recorded echoes was increased. TE values were adjusted as necessary to maintain curve accuracy [10].

All relaxation time measurements were performed in triplicate to ensure reproducibility. Statistical analysis was carried out using IBM SPSS Statistics v.26 software. The mean values and standard deviations were calculated for each set of measurements. One-way analysis of variance (ANOVA) was used to determine the statistical significance of differences in T_1 and T_2 relaxation times between water and glycerin samples. A significance level of $p < 0.05$ was used throughout. The coefficient of variation was also calculated to assess the consistency and reliability of the data [11].

3. Results and Discussion

The evaluation of the longitudinal relaxation time T_1 was carried out using a 10 mm thick water sample with a compact MR tomograph. To investigate the effect of the repetition time TR between two 90° RF pulses on the amplitude of the recorded signal, three series of measurements were conducted with different TR values. The results are presented in Figures 1–3.

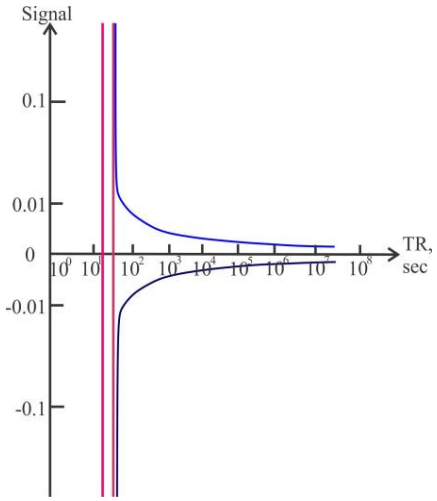

Figure 1 – Dependence of normalized signal amplitude on TR for a short value. The signal is minimal due to insufficient longitudinal magnetization recovery

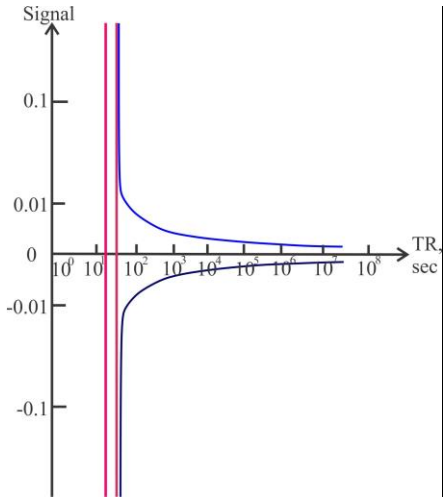

Figure 2 – Increase in signal amplitude with intermediate TR. Partial recovery of longitudinal magnetization leads to higher transverse signal

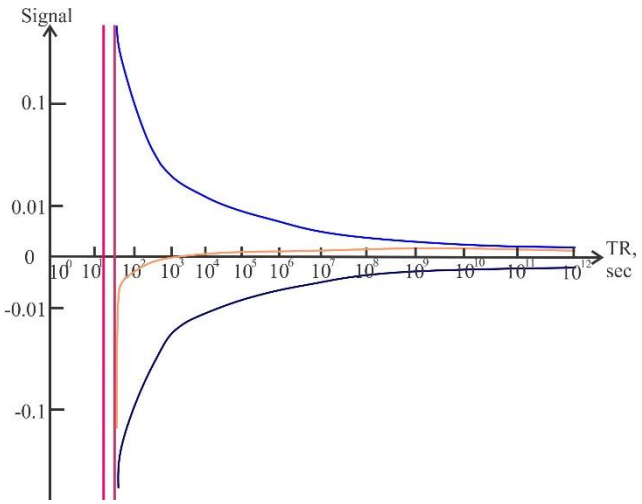

Figure 3 – Maximum signal amplitude observed at long repetition time $TR \approx 15$ s, indicating complete recovery of longitudinal magnetization

In Figure 1, the shortest repetition time resulted in the weakest signal, indicating that the longitudinal magnetization vector $\overrightarrow{M_L(t)}$ had not fully recovered along the direction of the external magnetic field $\overrightarrow{B_0}$. Consequently, the second 90° *RF* pulse could not effectively rotate the magnetization vector into the transverse plane, and the resulting transverse magnetization $\overrightarrow{M_Q(t)}$ was significantly reduced. This led to a decrease in the amplitude of the detected signal. These observations suggest that the longitudinal relaxation time T_1 of water is relatively long and exceeds 1 second.

Figures 2 and 3 show a progressive increase in signal amplitude with longer TR. At TR = 15 s, signal saturation was observed further increases in TR did not produce significant changes in amplitude. This indicates that at TR = 15 s, full recovery of the longitudinal magnetization had occurred, and the recorded signal amplitude corresponds to the system's maximum. To quantitatively estimate T_1, a method based on the half-recovery time of longitudinal magnetization was used. The experiment showed that at TR = 2 s, the signal amplitude was approximately 50% of the maximum recorded at TR = 15 s. This allowed for an approximate calculation of T_1 using the following equation:

$$T_1 = \frac{TR_{\frac{1}{2}}}{ln2} \quad (1)$$

When T_1 was abound of 2.9 s. This value aligns well with published data for water at room temperature and confirms the sensitivity of the method to the selection of TR in nuclear magnetic resonance measurements [6].

Figures 4 – 6 show the measured signal amplitude following the second 90° RF pulse for a 10 mm thick glycerin sample, under the same three TR conditions as those used for the water sample. In contrast to water, the signal amplitude remains nearly unchanged across all three TR values, indicating that glycerin reaches equilibrium magnetization significantly faster.

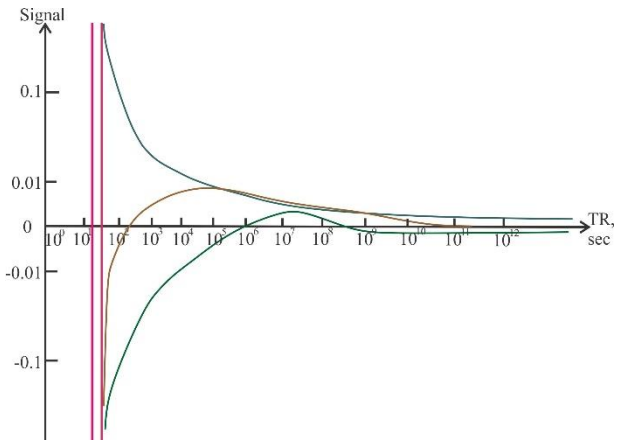

Figure 4 – Glycerin sample signal after second 90° RF pulse at short TR

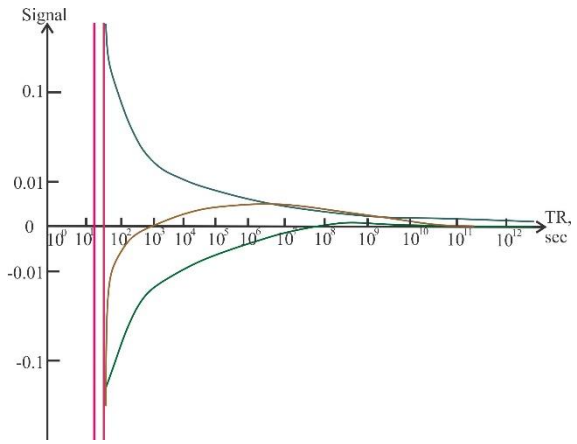

Figure 5 – Same signal at intermediate TR

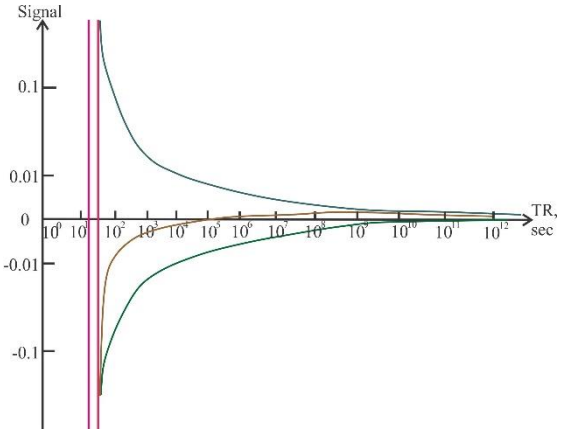

Figure 6 – Signal at long TR: no visible amplitude difference across all three

This observation suggests that the longitudinal magnetization vector in glycerin rapidly returns to a position nearly parallel to the external magnetic field $\overrightarrow{B_0}$, even at short repetition times. As a result, the second 90° RF pulse effectively rotates the magnetization vector into the transverse plane in all three cases, producing nearly identical transverse magnetization $\overrightarrow{M_Q(t)}$, and thus signal amplitude, regardless of *TR*. This indicates that the longitudinal T_1 of glycerin is much shorter compared to that of water.

To estimate the relaxation time, the same exponential recovery model Equation 1 was applied. The experiment revealed that the signal amplitude drops to approximately 50% of its maximum at *TR* ≈ 0.08 s. Therefore, the longitudinal relaxation time T_1 for glycerin can be calculated as ≈ 0.12 s.

This value reflects the high relaxation efficiency of glycerin, likely due to its higher viscosity and slower molecular motion compared to water, which enhances dipole-dipole interactions responsible for T_1 relaxation.

Moreover, the exponential relaxation curve for each substance was recorded and analyzed to evaluate the influence of repetition time, time step, and the number of data points on the accuracy and shape of the fitted T_1 relaxation curve (Figures 7 and 8).

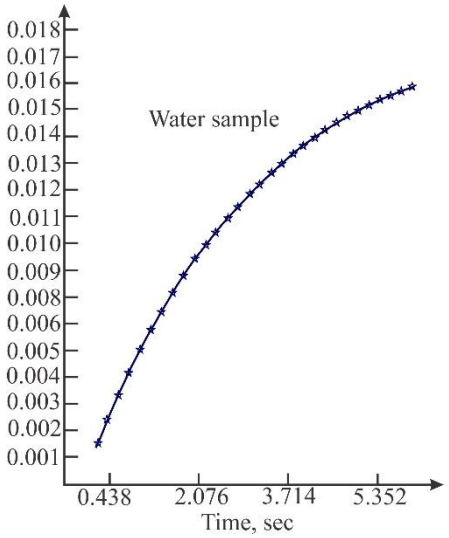

Figure 7 – Exponential approximation of the curve relaxation curve T_1 of water

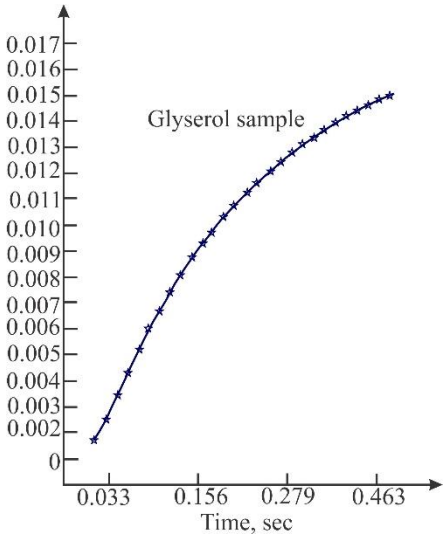

Figure 8 – Exponential FIT relaxation curve T_1 glycerol

The TR in this phase refers to the time between successive measurements, each formed by a pair of 90° RF pulses. To accurately capture the T_1 relaxation behavior, it is essential that TR be long enough to allow the spin ensemble to return nearly to thermal equilibrium before each new measurement. If TR is too short, the magnetization vector does not fully realign with the external magnetic field $\overrightarrow{B_0}$, and the first recorded signal of the sequence is weakened. Consequently, the second RF pulse within the same measurement results in an incomplete rotation of the magnetization vector into the transverse plane, leading to a distorted signal and an inaccurate representation of the T_1 relaxation curve. Although longer TR increases the total acquisition time, it is generally recommended that TR be at least three times longer than the estimated T_1 of the substance under investigation. At this point, approximately 95% of the longitudinal magnetization has recovered, ensuring valid signal formation.

The time step determines the increment between successive measurement intervals, i.e., the time difference between two 90° pulses in each consecutive measurement. A smaller time step enables more detailed scanning of the T_1 curve. However, to accurately describe the entire relaxation process, the scan must extend beyond the expected T_1 value.

For glycerin, the repetition time was set to 0.5 seconds, with 30 data points recorded at a time step of 15 ms. The measured data were fitted using the exponential function:

$$f(x) = a - b \cdot e^{-\frac{x}{T_1}} \quad (2)$$

yielding the following parameters a = 0.021; b = 0.023; T_1 = 126 ms. The close similarity between a and b confirms ideal excitation conditions using a 90° RF pulse. The determined relaxation time of 126 ms is consistent with the previously estimated value based on half-signal amplitude at $TR \approx 0.08$ s. The same procedure was applied to water. The repetition time was increased to 10 s, with 30 data points collected at a 200 ms time step. Using Eq. 2 has resulted in the a = 0.021; b = 0.021; T_1 = 3.0 3000 ms. As with glycerin, the equality of a and b confirms correct signal formation under 90° RF excitation. The relaxation time of 3.0 seconds further validates the findings of the earlier experiment based on *TR* variation and confirms that water has a substantially slower longitudinal relaxation process compared to glycerin.

Figure 7 presents the measured spin-echo decay curve for the glycerin sample. The vertical axis corresponds to the signal amplitude of each echo, while the horizontal axis shows the elapsed time in seconds. As expected, the signal exhibits an exponential decrease, characteristic of T_2 relaxation behavior. The high density of data points and minimal noise validate the measurement conditions and confirm the importance of short echo spacing and sufficient total sampling time.

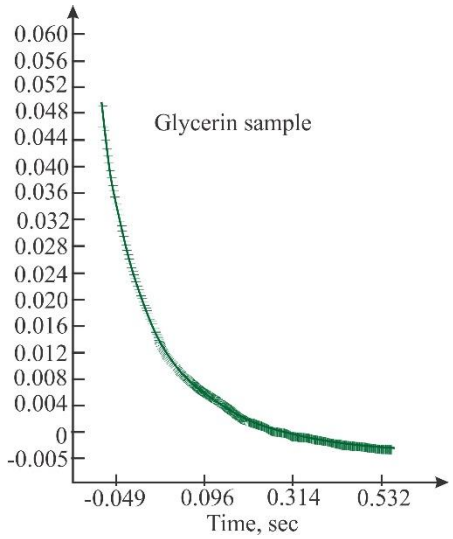

Figure 9 – Exponential FIT of the relaxation curve T_2 glycerol

This section of the experiment aimed to determine the transverse relaxation time T_2 of glycerin using a spin-echo sequence consisting of multiple echo signals. Each spin echo reflects the remaining $\overrightarrow{M_Q(t)}$, separated from the next by an echo time $T_E = \tau\Delta 180°$. Accurate scanning of the T_2 relaxation curve requires a large number of echoes and a short echo time to ensure high temporal resolution. If the echo time TE is selected incorrectly—i.e., too long—it can lead to artificial and undesirable dephasing effects due to limitations of the measurement sequence. These effects distort the relaxation process, resulting in underestimation of the true T_2 value. Therefore, echo time must be minimized to avoid coherence loss and to preserve the integrity of the transverse relaxation signal. Notably, unlike T_1 measurements which require multiple repetitions with different delay times, T_2 can be reliably determined in a single measurement using a continuous multi-echo sequence. In this experiment, the echo time was set to 2 ms and the number of echoes to 250, which enabled precise sampling of the decay curve. For glycerin, the fitted parameters were a = 0.052; c = 0.002; T_2 = 0.094 s. For water were a = 0.052; c = 0.002; $T_2 = 1.423$ s.

This much longer relaxation time reflects water's lower viscosity and faster molecular motion, which reduces dipole-dipole interaction efficiency and thereby extends transverse magnetization persistence. These results confirm the critical role of echo time and signal density in T_2 analysis and demonstrate that accurate values can be obtained through a single, well-designed multi-echo acquisition.

4. Conclusions

The longitudinal relaxation time T_1 for water was determined to be approximately 3.0 s, while for glycerin it was significantly shorter at 0.126 s, highlighting the effect of molecular mobility on relaxation behavior.

The transverse relaxation time T_2, obtained through a multi-echo sequence and exponential fitting, was measured as 1.423 s for water and 0.094 s for glycerin, confirming that glycerin exhibits faster signal decay due to its higher viscosity.

The study confirmed that accurate determination of T_1 requires a repetition time at least three times greater than the estimated relaxation time, and T_2 measurements demand short echo times and a high number of echoes for reliable exponential fitting.

The results addressed the core research problem by demonstrating how key acquisition parameters (repetition time, echo time, number of echoes) influence the accuracy of relaxation time measurements in NMR.

The findings can support future NMR-based characterization of complex fluids, aiding in the optimization of measurement protocols for different substances.

The primary constraint of this study was the limited range of tested substances. Further research should explore broader material categories and advanced fitting models to refine relaxation analysis.

References

[1] M. Goldman, "ADVANCES IN MAGNETIC RESONANCE Formal Theory of Spin-Lattice Relaxation," *J. Magn. Reson.*, vol. 149, pp. 160–187, 2001, doi: 10.1006/jmre.2000.2239.

[2] H. J. Mamin *et al.*, "Nanoscale nuclear magnetic resonance with a nitrogen-vacancy spin sensor," *Science (80-.).*, vol. 339, no. 6119, pp. 557–560, Feb. 2013, doi: 10.1126/SCIENCE.1231540/SUPPL_FILE/MAMIN.SM.PDF.

[3] S. C. L. Deoni, T. M. Peters, and B. K. Rutt, "Determination of optimal angles for variable nutation proton magnetic spin-lattice, T1, and spin-spin, T2, relaxation times measurement," *Magn. Reson. Med.*, vol. 51, no. 1, pp. 194–199, Jan. 2004, doi: 10.1002/MRM.10661.

[4] K. Li *et al.*, "Optimized inversion recovery sequences for quantitative T1 and magnetization transfer imaging," *Magn. Reson. Med.*, vol. 64, no. 2, pp. 491–500, 2010, doi: 10.1002/MRM.22440.

[5] S. Shin, S. D. Yun, and N. J. Shah, "T2* quantification using multi-echo gradient echo sequences: a comparative study of different readout gradients," *Sci. Reports 2023 131*, vol. 13, no. 1, pp. 1–14, Jan. 2023, doi: 10.1038/s41598-023-28265-0.

[6] D. Cicolari *et al.*, "A method for T1 and T2 relaxation times validation and harmonization as a support to MRI mapping," *J. Magn. Reson.*, vol. 334, p. 107110, Jan. 2022, doi: 10.1016/J.JMR.2021.107110.

[7] R. R. Ernst, G. Bodenhausen, and A. Wokaun, "Principles of Nuclear Magnetic Resonance in One and Two Dimensions," *Princ. Nucl. Magn. Reson. One Two Dimens.*, May 1990, doi: 10.1093/OSO/9780198556473.001.0001.

[8] D. A. Barskiy *et al.*, "Zero- to ultralow-field nuclear magnetic resonance," *Prog. Nucl. Magn. Reson. Spectrosc.*, vol. 148–149, p. 101558, Aug. 2025, doi: 10.1016/J.PNMRS.2025.101558.

[9] Y. Luo *et al.*, "Deep learning and its applications in nuclear magnetic resonance spectroscopy," *Prog. Nucl. Magn. Reson. Spectrosc.*, vol. 146–147, p. 101556, Apr. 2025, doi: 10.1016/J.PNMRS.2024.101556.

[10] D. E. Demco, A. M. Oros-Peusquens, and N. J. Shah, "Nonlinear effects in magnetic resonance localized spectroscopy and images," *Prog. Nucl. Magn. Reson. Spectrosc.*, vol. 146–147, p. 101557, Apr. 2025, doi: 10.1016/J.PNMRS.2025.101557.

[11] R. Y. Hwang *et al.*, "Measuring the water content of polymer electrolyte membranes using double points of proton magic angle spinning nuclear magnetic resonance data," *Polymer (Guildf).*, vol. 309, p. 127431, Sep. 2024, doi: 10.1016/J.POLYMER.2024.127431.

Information about authors:

Aigul Akkulova – MS, Research Assistant, The computational materials science laboratory, National Laboratory Astana, Astana, Kazakhstan, aigul.akkulova@mail.ru

Author Contributions:

Aigul Akkulova – concept, methodology, resources, data collection, testing, modeling, analysis, visualization, interpretation, drafting, editing, funding acquisition.

Conflict of Interest: The authors declare no conflict of interest.

Use of Artificial Intelligence (AI): The authors declare that AI was not used.

Received: *05.02.2025*
Revised: 16.03.2025
Accepted: 18.03.2025
Published: 21.03.2025

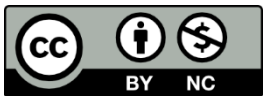

Technobius Physics, 2025, 3(1), 0028, DOI: https://doi.org/10.54355/tbusphys/3.1.2025.0028

Technobius Physics

https://technobiusphysics.kz/

e-ISSN 3007-0147

Article

Experimental determination of X-ray absorption and K-edge behavior in metal foils

Sanzhar Serik*

Department of Physics, School of Science and Humanities, Nazarbayev University, Astana, Kazakhstan
*Correspondence: sanzhar.serik.00@bk.ru

Abstract. This study investigates the absorption behavior of X-rays in various metallic foils, focusing on the dependence of transmitted intensity and mass attenuation coefficient (μ/ρ)s on material thickness and radiation wavelength. The objective was to experimentally validate theoretical models of X-ray attenuation and to determine the position of K absorption edges for selected elements. Using a goniometer-based X-ray setup equipped with a Geiger-Müller counter, a series of measurements were conducted on aluminum, zinc, tin, copper, and nickel foils under controlled conditions. The first part of the experiment demonstrated an exponential decrease in transmitted intensity with increasing absorber thickness. The second part established a cubic dependence of the mass attenuation coefficient (μ/ρ)on the wavelength of the incident X-rays, consistent with theoretical expectations for photoelectric absorption. In the third part, distinct K absorption edges were successfully identified for copper and nickel, with experimentally determined edge energies closely matching known values. The results confirmed that materials with higher atomic numbers exhibit greater absorption and sharper K-edges. Minor deviations observed near absorption thresholds were attributed to spectral interference and detector resolution limitations. Overall, the study validated key theoretical relationships and demonstrated the effectiveness of the experimental setup for accurately characterizing X-ray absorption behavior in metals.
Keywords: X-ray absorption, mass attenuation, K-edge detection, metal foils, wavelength dependence.

1. Introduction

X-ray absorption is a fundamental interaction between high-energy photons and matter, characterized by a reduction in intensity as X-rays pass through different media. This phenomenon underpins numerous applications, including non-destructive testing, medical diagnostics, and elemental analysis. A key parameter in quantifying this interaction is the mass attenuation coefficient $\sqrt[3]{\mu/p}$, which depends on the atomic number Z, density, and photon energy or wavelength of the incident radiation. The primary mechanism governing absorption in this context is the photoelectric effect, particularly dominant at lower photon energies and in materials with higher atomic numbers.

Accurate determination of $\sqrt[3]{\mu/p}$ is essential for practical applications involving shielding design, spectroscopic material analysis, and imaging systems calibration. Although theoretical models predict an inverse cubic relationship with photon energy, experimental validation remains critical, especially near sharp absorption edges such as the K-edge, where the incident photon energy becomes sufficient to eject core electrons.

Recent studies have refined the experimental measurement of mass attenuation coefficients. The authors developed a versatile laboratory X-ray absorption spectrometer capable of multi-mode detection and demonstrated accurate edge resolution for several metals [1]. In another study, authors provided experimentally measured attenuation coefficients for elements ranging from low to medium atomic numbers, identifying deviations in regions close to absorption edges [2]. Scientists investigated energy-dependent attenuation in various alloys and confirmed that deviations from

theoretical predictions occur due to structural variations in crystalline materials [3]. Furthermore, researchers presented comprehensive data for transition metals, validating the dependence of $\sqrt[3]{\mu/p}$ on λ^3 and identifying systematic differences near absorption thresholds [4]. These investigations collectively highlight both progress and remaining limitations in achieving high precision near abrupt energy transitions.

Despite these advances, existing studies often focus on isolated materials or energy ranges, limiting the ability to generalize results across a broad set of metals under unified experimental conditions. Moreover, practical constraints such as spectral overlap, detector resolution, and second-order interference continue to affect the accuracy of K-edge determination.

To address this gap, we hypothesize that by employing a calibrated goniometer-based experimental chamber with a Geiger-Müller (GM) detector, it is possible to experimentally verify theoretical models of X-ray attenuation and accurately determine the mass attenuation coefficients and K-edge energies for a range of metals. Specifically, we anticipate confirming the exponential attenuation of X-ray intensity with absorber thickness, the cubic dependence of $\sqrt[3]{\mu/p}$ on wavelength, and the identification of element-specific K-edges.

The objective of this study is to experimentally determine the mass attenuation coefficient $\sqrt[3]{\mu/p}$ for aluminum, zinc, tin, copper, and nickel as functions of both material thickness and incident X-ray wavelength. This work combines three structured experimental tasks into a unified investigation, aiming to validate key theoretical relationships and improve the reliability of educational and practical X-ray absorption measurements. The novelty lies in its comprehensive, comparative approach using a consistent apparatus setup across all materials.

2. Methods

X-ray absorption experiments were conducted using a standard goniometer-based experimental chamber equipped with an analyser crystal and a GM counter tube. The goniometer (by Leybold Company P2540105) was connected to the X-ray unit and the counter tube via dedicated sockets. The analyser crystal was mounted at the terminal position on the right-hand rail, and the GM counter was fixed to the back stop using a standard holder. A diaphragm was placed in front of the GM tube to limit background radiation, while a 2 mm diaphragm tube was inserted into the beam outlet of the X-ray tube plug-in unit. The X-ray system was connected to a computer via USB for data acquisition and control.

For absorption of X-rays as a function of material thickness foils of aluminium and tin with varying thicknesses were inserted manually into the diaphragm in front of the GM counter. Two characteristic glancing angles were selected to represent both characteristic line emission and bremsstrahlung regions: 20.4° for the copper Kβ line and ~10° for bremsstrahlung. For each selected angle, the intensity was recorded without absorber (I_0) and with the foil absorber (I), using a gate timer with an integration time of 50 s. To improve statistical reliability and minimize relative errors, measurements were conducted until the pulse rate was below 1000 counts per second. Data were collected for single foils and for paired foils to simulate increased absorber thickness.

For determination of the mass absorption coefficient as a function of wavelength absorption spectra were recorded using aluminium (d = 0.08 mm) and tin (d = 0.025 mm) foils separately. For each material, glancing angles were scanned in the range of 6° to 16° with steps of 1–2°, while maintaining a minimum integration time of 50 s. A reference spectrum (I_0) without any absorber was also recorded under identical conditions. Using Bragg's law, the glancing angles were converted to corresponding wavelengths (λ), and the mass absorption coefficients (μ/ρ) were calculated by evaluating the transmission ratio I/I_0 and applying the Beer–Lambert law [5].

For determination of the absorption coefficient for copper and nickel a similar procedure was followed using copper and nickel foils (d = 0.025 mm), with spectra recorded over a wider angular range of 6°–25°, using 1° steps. In regions near the absorption edges, finer angular steps (<1°) were applied to accurately capture rapid changes in absorption. While the default anode voltage was 35

kV, improved spectral resolution was achieved at 20–25 kV by increasing integration times accordingly. The resulting data were used to plot absorption coefficients as a function of the wavelength of primary radiation.

All measurements were conducted under stable environmental conditions, and each dataset was statistically analysed using OriginPro 2021 software. The coefficient of variation was computed to assess the reproducibility of intensity measurements.

3. Results and Discussion

Figure 1 presents the measured ratio of transmitted to initial intensity ($\frac{I}{I_0}$) as a function of absorber thickness *d* for aluminium and zinc foils of varying thicknesses.

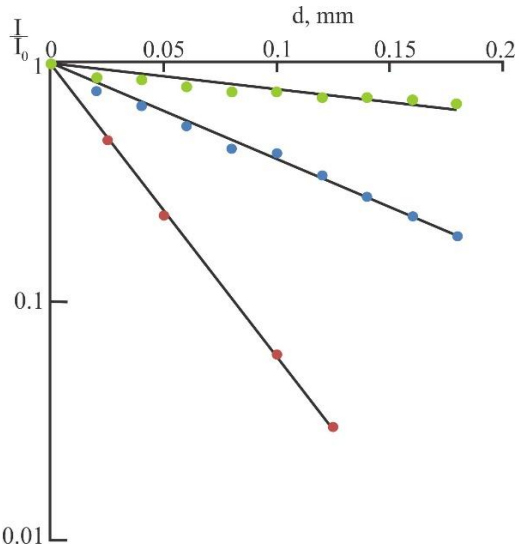

Figure 1 – Semi-logarithmic representation of the quotient as a function of the absorber thickness d

In Figure 1, three distinct exponential decay curves are observed. Curves 1 and 2 correspond to aluminium (Z = 13, ρ = 2.70 g/cm³), while curve 3 corresponds to zinc (Z = 30, ρ = 7.14 g/cm³). As the absorber thickness increases, the relative transmitted intensity $\frac{I}{I_0}$ decreases exponentially, consistent with the Beer–Lambert law [5]. The attenuation is significantly stronger for zinc than for aluminium, confirming the well-known dependence of X-ray absorption on atomic number Z.

Comparing curves 1 and 3 at the same primary radiation energy, zinc demonstrates a markedly higher absorption capacity. Additionally, comparing curves 1 and 2 for aluminium under different glancing angles (i.e., different radiation energies), a decrease in absorption is noted at higher photon energies. These observations are in agreement with theoretical predictions, where absorption is directly related to Z and inversely to photon energy. The complete dataset derived from these measurements is provided in Table 1.

Table 1 – Dependence of the absorption on the wavelength

Al (Z = 13)	μ, cm^{-1}	$d_{1/2}$, cm	$\frac{\mu}{\rho}$, $cm^2 g^{-1}$
ρ = 2.7 g/cm^3			
λ = 139 pm	112	$6.2 \cdot 10^{-3}$	41.5
λ = 70 pm	14.1	20.4	5.2
Zn (Z = 30)			
ρ = 7.14 g/cm^{-3}			
λ = 139 pm	280	$2.5 \cdot 10^{-3}$	39.2

These results reinforce the understanding that higher-Z materials more effectively attenuate X-rays and that attenuation diminishes with increasing photon energy. However, as the primary radiation energy lies within the K-edge of zinc, the simplified Z-dependence of the mass absorption coefficient is not fully applicable in this region.

Figure 2 illustrates the cubic root of the mass absorption coefficient $(\mu/\rho)^3$ as a function of the X-ray wavelength (λ) for aluminium and tin foils, each with a fixed thickness.

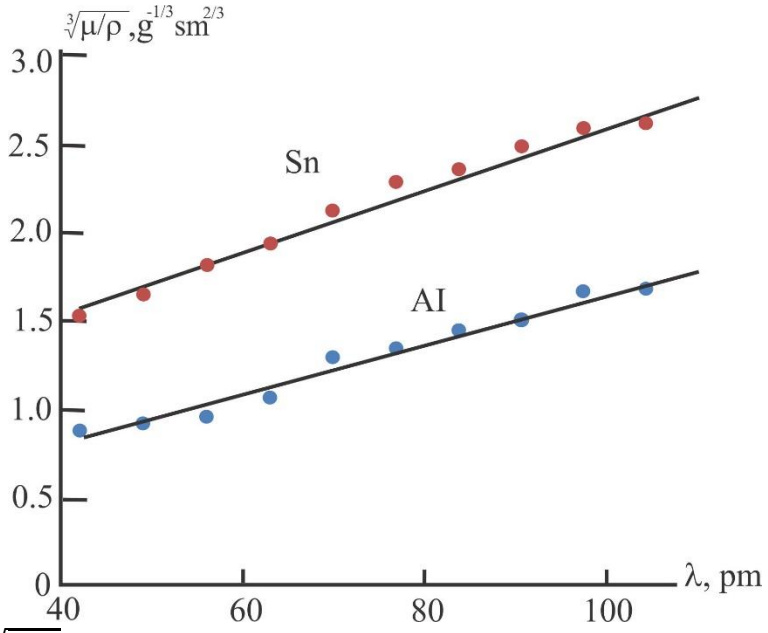

Figure 2 – $\sqrt[3]{\mu/p}$ for aluminium and tin as a function of the primary radiation energy

After converting glancing angles to wavelengths using Bragg's law [5], the experimental data were processed to determine $\sqrt[3]{\mu/p}$ for each material. The plotted values of $\sqrt[3]{\mu/p}$ against λ demonstrate a clear linear trend for both aluminium and tin, confirming the theoretical dependence with a higher atomic number (Z = 50, ρ = 7.28 g/cm³), consistently exhibits greater absorption values compared to aluminium, as reflected by the higher position of its trend line. These linear dependencies validate the suitability of the Beer–Lambert model and confirm that the dominant absorption mechanism in this range is photoelectric in nature, where the absorption cross-section increases steeply with decreasing photon energy and increasing atomic number. The trends observed in both experiments strongly support classical X-ray absorption theory. The exponential decrease of transmitted intensity with thickness (Figure 1) aligns with expectations from fundamental attenuation laws, while the wavelength-dependence of μ/ρ (Figure 2) is consistent with the known power-law behavior for photoelectric absorption. The strong dependence on Z is also clearly visible when comparing aluminium, tin, and zinc. These findings are consistent with prior experimental studies [6], [7], confirming the reliability of the experimental setup and procedure.

Minor deviations from ideal exponential behavior at certain wavelengths may be attributed to proximity to absorption edges or instrumental limitations, including GM tube response time or diaphragm alignment. For future experiments, finer step sizes near K-edges and higher-resolution detectors could improve precision.

Figures 3 and 4 show the cubic root of the mass absorption coefficient $\sqrt[3]{\mu/p}$ as a function of the X-ray wavelength λ for copper and nickel foils, respectively.

In both graphs, a linear correlation between $\sqrt[3]{\mu/p}$ and λ is evident in the region where $\lambda \neq \lambda_K$. However, near the so-called *K* absorption edge ($\lambda = \lambda_K$), a distinct discontinuity occurs. This jump corresponds to the photon energy surpassing the binding energy of the K-shell electrons, enabling photoionization. For copper (Z = 29, ρ = 8.96 g/cm³), this edge appears at λ_K = 138 pm, while for nickel (Z = 28, ρ = 8.99 g/cm³), the edge is at λ_K = 149 pm.

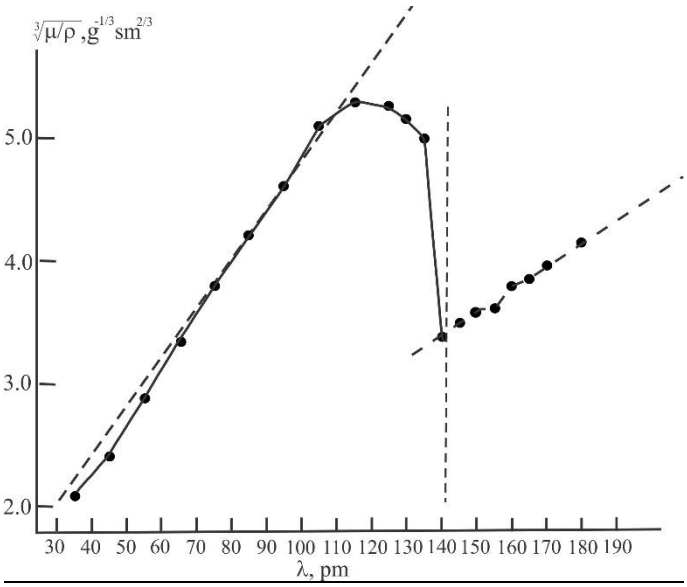

Figure 3 – Absorption edge of Cu: U_A =25 kV, λ_K =138 pm

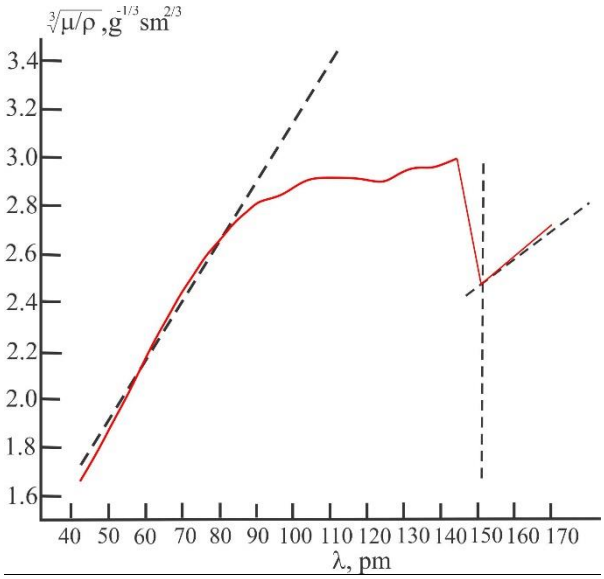

Figure 4 – Absorption edge of Ni: U_A =25 kV, λ_K =149 pm

Below these thresholds (λ < 70 pm), both curves deviate from linearity due to increased intensity of the primary radiation from second-order diffraction or interference effects. According to the Bragg condition for cooper λ_K=138 pm → E_K = 8.98 keV and for nickel λ_K=149 pm → E_K = 8.32 keV. These values confirm the accuracy of the experiment. Since $Z_{Ni} < Z_{Cu}$, the absorption edge for nickel occurs at a longer wavelength and lower energy than for copper, as expected.

The trends in Figures 3 and 4 are consistent with classical X-ray absorption theory. A linear relationship between $\sqrt[3]{\mu/p}$ and λ is valid outside the absorption edge, confirming the proportionality $\mu/\rho \propto \lambda^3$. A sharp increase in absorption at $\lambda = \lambda_K$ is a characteristic feature of K-edge transitions. The difference in λ_K between copper and nickel correlates with their atomic numbers, validating the theoretical expectation that higher-Z elements have lower λ_K and higher K-shell binding energies. These results confirm that the mass absorption coefficient is strongly dependent on both wavelength and atomic structure. The deviation from linearity at shorter wavelengths is attributed to higher-order harmonics in the bremsstrahlung spectrum, which lead to overestimated transparency of the absorber.

4. Conclusions

The study successfully investigated the absorption behavior of X-rays as a function of material thickness and wavelength for aluminium, tin, copper, and nickel foils using GM detection and goniometer-based measurements. An exponential decrease in transmitted intensity $\frac{I}{I_0}$ with increasing absorber thickness was observed, confirming the Beer–Lambert law. Zinc exhibited significantly higher absorption than aluminium at equal thicknesses due to its higher atomic number (Z = 30; Z = 13). A linear relationship between $\sqrt[3]{\mu/p}$ and wavelength λ was confirmed for aluminium and tin, supporting the empirical law $\mu/\rho \propto \lambda^3$. Tin showed greater absorption than aluminium due to its higher Z (Z = 50; Z = 13). Distinct K absorption edges were identified for copper (λ_K=138 pm → E_K = 8.98 keV) and nickel (λ_K=149 pm → E_K = 8.32 keV), in agreement with theoretical expectations based on atomic number.

The study addressed the research objective by demonstrating the dependence of X-ray absorption on both absorber thickness and primary radiation wavelength, and by quantitatively determining the absorption edge energies. The results may be used in educational settings to demonstrate X-ray absorption principles or in material identification based on spectral edge analysis. Limitations include spectral resolution near absorption edges and second-order interferences at short

wavelengths. Further studies may involve higher-resolution detectors and more precise step sizes around λ_K to improve accuracy.

References

[1] G. Bunker, "X-ray absorption spectrometers," *Encycl. Spectrosc. Spectrom.*, pp. 610–616, Jan. 2016, doi: 10.1016/B978-0-12-409547-2.05066-6.
[2] R. Hauko, J. P. Gomilšek, I. Arčon, and A. Kodre, "Absolute determination of the x-ray absorption coefficient of strontium in the K edge region," *Radiat. Phys. Chem.*, vol. 103, pp. 203–208, 2014, doi: 10.1016/J.RADPHYSCHEM.2014.05.059.
[3] O. Paul, S. Toscano, K. Totland, and M. Landolt, "The spatial origin of the spin-polarization of secondary-electron emission from Fe," *Surf. Sci.*, vol. 251–252, no. C, pp. 27–30, Jul. 1991, doi: 10.1016/0039-6028(91)90947-Q.
[4] M. T. Murphy and J. C. Berengut, "Laboratory atomic transition data for precise optical quasar absorption spectroscopy," *Mon. Not. R. Astron. Soc.*, vol. 438, no. 1, pp. 388–411, 2014, doi: 10.1093/MNRAS/STT2204.
[5] L. Li *et al.*, "Study on the origin of linear deviation with the Beer-Lambert law in absorption spectroscopy by measuring sulfur dioxide," *Spectrochim. Acta - Part A Mol. Biomol. Spectrosc.*, vol. 275, Jul. 2022, doi: 10.1016/J.SAA.2022.121192.
[6] Y. Sun, R. Hong, C. Tao, and D. Zhang, "Design and Optical Field Tuning of ITO Multi-Layer Films Based on Tamm Plasmon Effect," *Zhongguo Jiguang/Chinese J. Lasers*, vol. 51, no. 22, Nov. 2024, doi: 10.3788/CJL240479.
[7] W. Lu *et al.*, "Recent progress of multilayer composite transparent conductive film," *Kexue Tongbao/Chinese Sci. Bull.*, vol. 62, no. 5, pp. 372–384, Feb. 2017, doi: 10.1360/N972016-01133.

Information about authors:
Sanzhar Serik – MS, Research assistant, Department of Physics, School of Science and Humanities, Nazarbayev University, Astana, Kazakhstan, sanzhar.serik.00@bk.ru

Author Contributions:
Sanzhar Serik – concept, methodology, resources, data collection, testing, modeling, analysis, visualization, interpretation, drafting, editing, funding acquisition.

Conflict of Interest: The authors declare no conflict of interest.

Use of Artificial Intelligence (AI): The authors declare that AI was not used.

Received: 15.02.2025
Revised: 24.02.2025
Accepted: 25.03.2025
Published: 29.03.2025

Technobius Physics, 2025, 3(1), 0029, DOI: https://doi.org/10.54355/tbusphys/3.1.2025.0029

Technobius Physics

https://technobiusphysics.kz/

e-ISSN 3007-0147

Article

Pulsed cathodoluminescence of BaFBr crystals irradiated by swift heavy ions

Daurzhan Kenbayev[1,*], Elena Polisadova[2], Alexei Shalayev[3], Marina Konuhova[4]

[1]Department of Physics and Informatics, Shakarim University, Semey, Kazakhstan
[2]Department of Materials Science, National Research Tomsk Polytechnic University, Tomsk, Russian Federation
[3]Laboratory "Physics of single crystals", Vinogradov Institute of Geochemistry , Irkutsk, Russian Federation
[4]Institute of Solid State Physics, Riga, Latvia

*Correspondence: d.kenbayev@shakarim.kz

Abstract. This study investigates the influence of swift heavy ion irradiation on the pulsed cathodoluminescence properties of BaFBr crystals. The objective is to analyze how ion species and fluence affect exciton luminescence behavior under pulsed electron beam excitation. BaFBr crystals were irradiated with 147 MeV krypton and 227 MeV xenon ions at varying fluences, and their PCL spectra were recorded at room temperature. Time-resolved measurements revealed the presence of luminescence bands centered at 4.2 eV, attributed to self-trapped excitons. A comparative analysis of irradiated and unirradiated samples showed that ion irradiation led to notable modifications in the intensity and decay dynamics of the nanosecond and microsecond components of the emission. The fast component dominated at lower fluences, while higher fluences induced a shift toward slower decay processes, likely due to the accumulation of radiation-induced defects. The experimental results suggest that controlled ion irradiation can be used to tailor the luminescence characteristics of BaFBr crystals, with implications for improving materials used in digital imaging and radiation detection technologies.

Keywords: BaFBr, luminescence, pulsed cathodoluminescence, pulsed electron flow, fast heavy ions.

1. Introduction

Barium fluorobromide (BaFBr) is a mixed halide crystal known for its application in image plate technology due to its ability to store and release optical signals upon stimulation. Crystallizing in a tetragonal PbFCl-type structure, BaFBr is characterized by its layered nature and capacity to form self-trapped excitonic states upon irradiation or stimulation. Its exceptional performance as an X-ray storage phosphor, particularly when doped with Eu^{2+}, makes it highly relevant for use in digital radiography and dosimetry. Understanding the luminescence behavior of this material under various excitation conditions is crucial for improving image quality and detection sensitivity in pulsed radiographic systems.

Despite the technological importance of BaFBr-based phosphors, a comprehensive understanding of the luminescence mechanisms—particularly those involving self-trapped excitons (STEs)—remains elusive. The processes of energy storage and release involve complex electronic transitions and defect dynamics, especially under high-energy excitation or irradiation. Recent advances in radiation detection demand materials that can reliably function under extreme conditions, such as exposure to swift heavy ions (SHIs), yet the influence of such irradiation on the time-resolved luminescence characteristics of BaFBr is not fully understood.

Several studies have attempted to elucidate the mechanisms underlying luminescence in BaFBr. For instance, [1] investigated phonon and electronic transport in related systems, indirectly contributing to the understanding of energy transfer in irradiated crystals. [2] discussed strategies for

controlling thermal conduction in crystalline materials, a key factor in luminescent efficiency. More directly relevant, [3] examined electron-phonon interactions in semiconductors, offering insights into scattering mechanisms that may also govern exciton behavior in BaFBr. However, these studies either focus on different material systems or do not explicitly address the influence of ion irradiation on the luminescence decay dynamics of BaFBr.

The lack of targeted experimental data on the pulsed cathodoluminescence (PCL) behavior of BaFBr under high-energy ion bombardment represents a significant research gap . Previous work has largely overlooked how ion species, energy levels, and fluences modulate the temporal characteristics of excitonic emission, especially in the nanosecond to microsecond range. Moreover, the interplay between induced defects and exciton localization, which ultimately affects the emission decay kinetics, remains insufficiently characterized [4], [5], [6].

Based on these gaps, we hypothesize that irradiation with fast heavy ions (specifically Kr and Xe at energies of 147 and 227 MeV, respectively) significantly alters the PCL behavior of BaFBr crystals by modifying defect landscapes and affecting the balance between fast and slow excitonic decay components. This alteration can be quantitatively analyzed through time-resolved luminescence spectroscopy under pulsed electron beam excitation at room temperature.

The goal of this study is to investigate how swift heavy ion irradiation influences the spectral and temporal properties of pulsed cathodoluminescence in BaFBr crystals. By comparing irradiated and unirradiated samples across different ion species and fluences, we aim to identify key trends in exciton dynamics and define the role of induced defect states. The novelty of this work lies in its detailed analysis of PCL decay kinetics, using nanosecond-resolution time-resolved spectroscopy to reveal radiation-induced changes in the excitonic landscape of BaFBr crystals—a topic with direct implications for the development of advanced imaging phosphors and radiation detection materials.

In this work we present results on the exciton luminescence attenuation in barium fluorobromide crystals unirradiated and irradiated with 147 meV K and 227 MeV Xe ions up to fluences (10^{10}-10^{14}), (10^{10}-10^{12}) ion/cm^2, respectively, under excitation by pulsed electron flux at room temperature.

2. Methods

BaFBr crystals were grown by the Shteber method (Vinogradov Institute of Geochemistry SB RAS, Irkutsk, RF), in a graphite crucible in helium-fluoride atmosphere using stoichiometric mixtures of $BaBr_2$ and BaF_2.

Elemental analyses were performed by energy-dispersive X-ray spectroscopy (EDX or EDS) using an SEM Hitachi TM3030 (Hitachi High - Technologies Corporation, Tokyo, Japan) with a Bruker attachment and software quantax 70 (Bruker Nano GmbH, Berlin - Germany) EDX analysis. EDX is a method used to identify the composition of solid materials. This technique relies on exciting electrons close to the nucleus, which then causes distant electrons to lower their energy levels to fill the resulting holes. Each element releases a different set of X-ray frequencies when filling these holes, which can provide both qualitative and quantitative information about the near-surface composition of a sample.

The plate-shaped samples prepared for irradiation were approximately 1 mm thick. Irradiation was carried out at the heavy ion gas pedal DC-60 (Astana, Kazakhstan) by high-energy krypton ions with energy 147 MeV up to fluences: 10^{10}-10^{14} ions/cm^2 and xenon ions with 227 MeV energy up to fluences of 10^{10}-10^{12} ions/cm^2 at room temperature.

Pulsed cathodoluminescence (PCL) was excited by a pulsed electron beam by the accelerator GIN-600 with parameters: E = 0.25 MeV, $t_{1/2}$ = 15 ns, P_p = 40 mJ/cm^2. The spectra were measured on an optical spectrometer consisting of MDR-3 monochromator, PEM-97 photomultiplier tube, and a four-channel 350 MHz oscilloscope LeCroy WR 6030A. Luminescence oscillograms were recorded for photons with a certain energy between 1.0 and 5.0 eV at room temperature. The oscillograms were then converted into luminescence kinetic curves to determine the luminescence attenuation

parameters and record the luminescence spectrum at a given time delay with a time resolution of 7ns statistical processing of data was carried out in the OriginPro program.

3. Results and Discussion

The spectrum of pulsed cathodoluminescence of unirradiated and irradiated crystals consists of a band with a maximum in the region of 4.2 eV, which, according to [7], corresponds to the luminescence of an self -trapped exciton (STE) of bromine. In [8], the authors hypothesized that the STE in BaFBr crystals has a two-center type structure consisting of an electron and a self-trapped hole $V_k(Br_2^-)$.

In each of the studied samples irradiated with krypton ions, a gradual decrease in intensity and a change in the shape of the luminescence curve in the ultraviolet region of the spectrum can be traced. According to the graphs shown in Figures 1 and 2, the dependence of the band intensity (PCL) 4.2 eV, on the fluence at irradiation with fast heavy ions ^{84}Kr and ^{130}Xe can be traced. The nanosecond component of the pulsed cathodoluminescence spectra flares up to fluence $1x10^{12}$ ions/cm^2 followed by slow decay up to fluence $1x10^{14}$ ions/cm^2, the microsecond component is not subject to noticeable intensity changes depending on the absorbed irradiation dose.

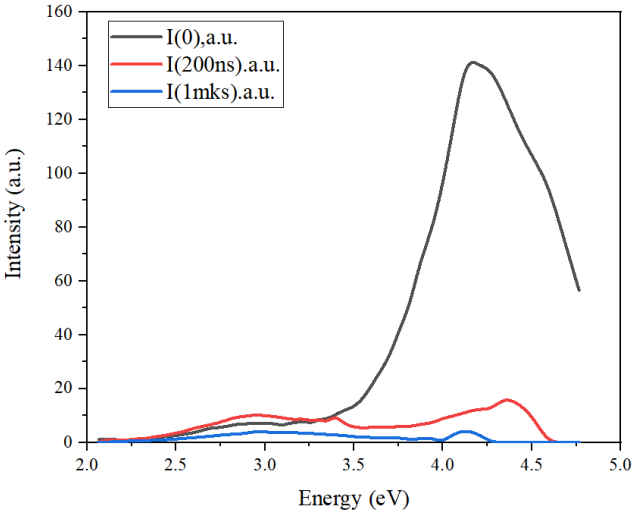

a) Unirradiated sample

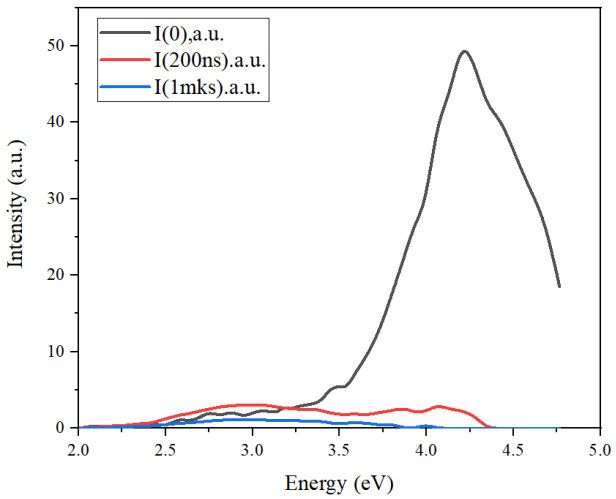

b) fluence $1x10^{10}$ ions/cm^2

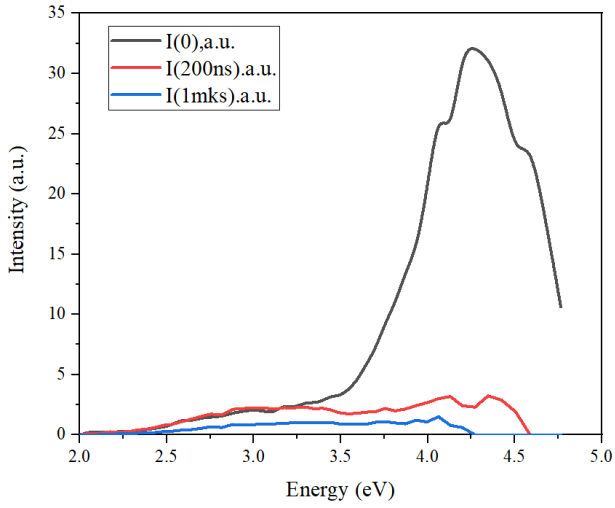

c) fluence $1x10^{11}$ ions/cm^2

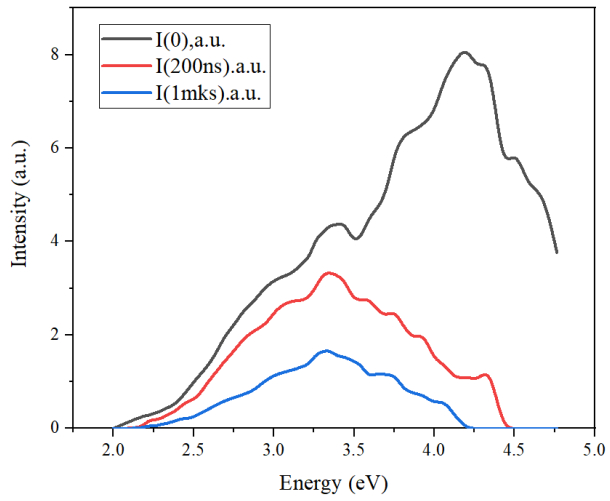

d) fluence $1x10^{12}$ ions/cm^2

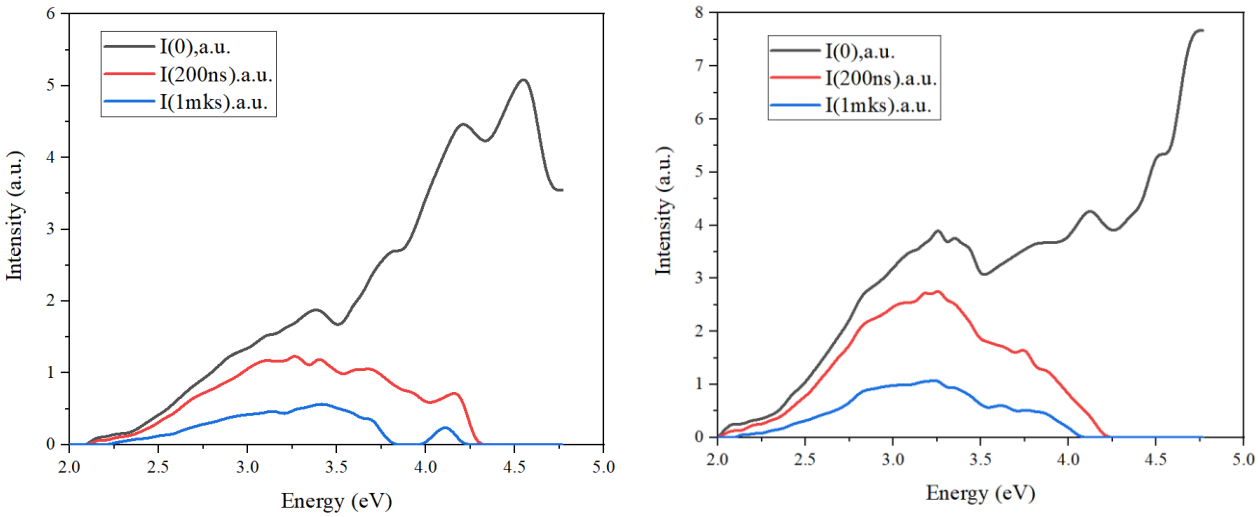

e) fluence $1x10^{13}$ ions/cm^2 f) fluence $1x10^{14}$ ions/cm^2

Figure 1 – Spectra of microsecond (blue curve) and nanosecond (red curve) attenuation components of pulsed cathodoluminescence of BaFBr crystals irradiated with ^{84}Kr ions, E=147 MeV to fluences of $1x10^{10}$ - $1x10^{14}$ ions/cm^2 at room temperature

A distinctive characteristic of the 4.2 eV luminescence band is its good intensity at temperatures much higher than 77K. The data obtained by measuring pulsed cathodoluminescence at room temperature clearly demonstrate this (Figure 1a). According to [9], this band may originate from perturbed STE near point defects or impurity ions and arise according to the scheme "F+$V_k(Br_2^-)$" with the neighboring impurity ion O^{2-}.

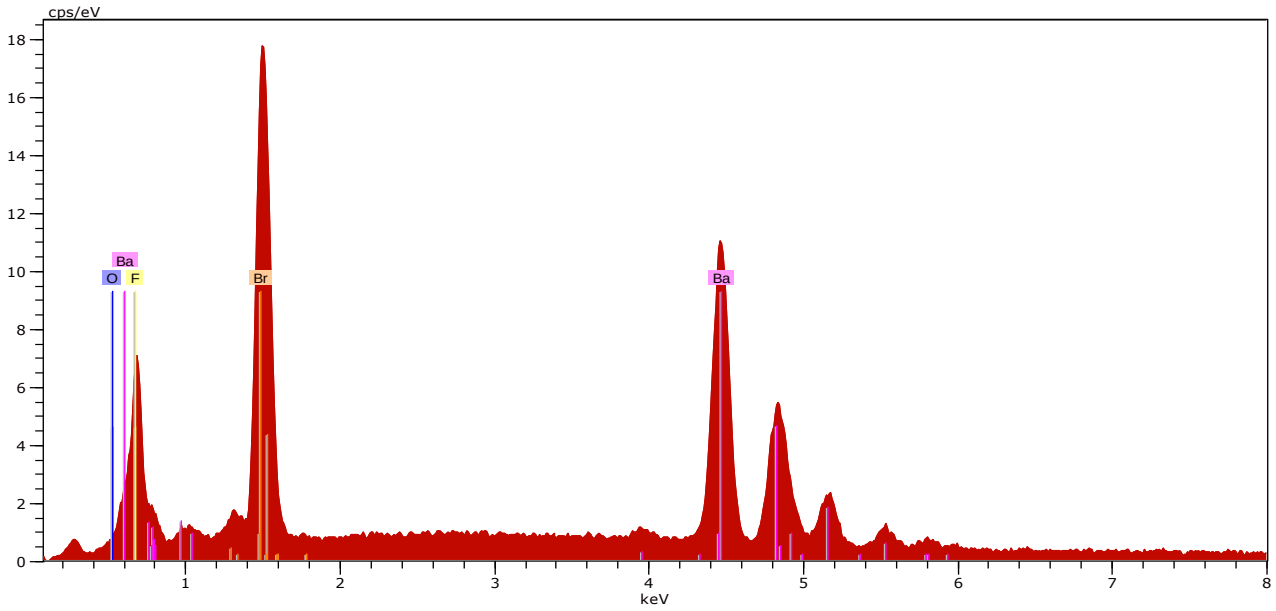

Figure 2 – EDX analyses for BaFBr

It should be noted that the BaFBr crystal contains some amount of oxygen O^{2-} on the crystal surface, this is evident from the data carried out by elemental dispersion analysis on the composition (Figure 2).

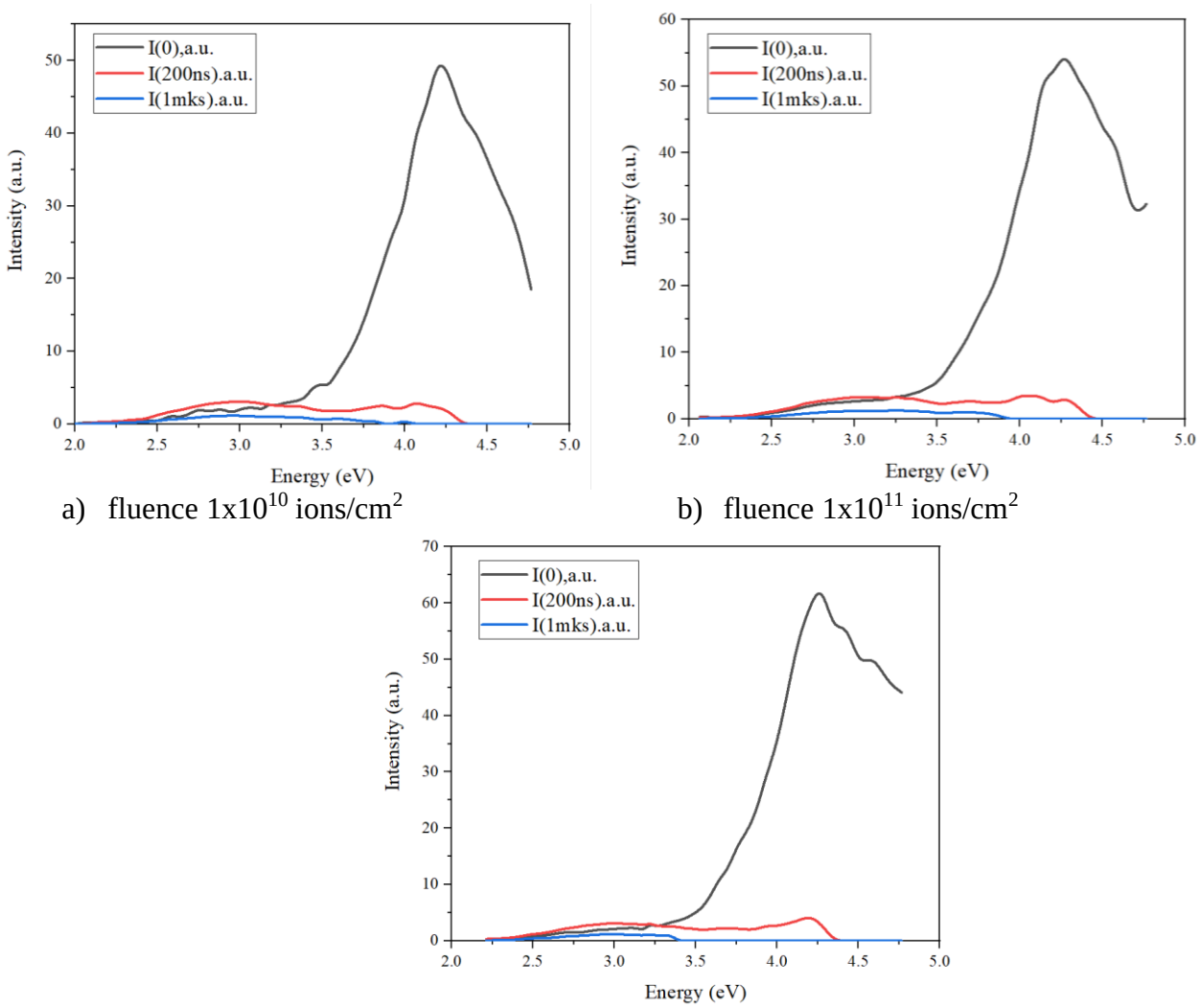

a) fluence $1x10^{10}$ ions/cm^2 b) fluence $1x10^{11}$ ions/cm^2

c) fluence $1x10^{12}$ ions/cm^2

Figure 3 – Spectra of microsecond (blue curve) and nanosecond (red curve) decay components of pulse cathodoluminescence attenuation of BaFBr crystals irradiated with ^{130}Xe ions, E=227 MeV to fluences of $1x10^{10}$ - $1x10^{12}$ ions/cm^2 of unalloyed BaFBr crystal, at room temperature

In BaFBr crystals irradiated with xenon ions, the glow of autolocalized bromine excitons and the flaring of the nanosecond component are also observed. It is noteworthy that at high fluences of $1x10^{13}$-$2x10^{13}$ ion/cm^2 the crystal began to peel and collapse, most likely this is due to track overlap [10]. The attenuation curves of the studied samples are shown in Figure 4a – i.

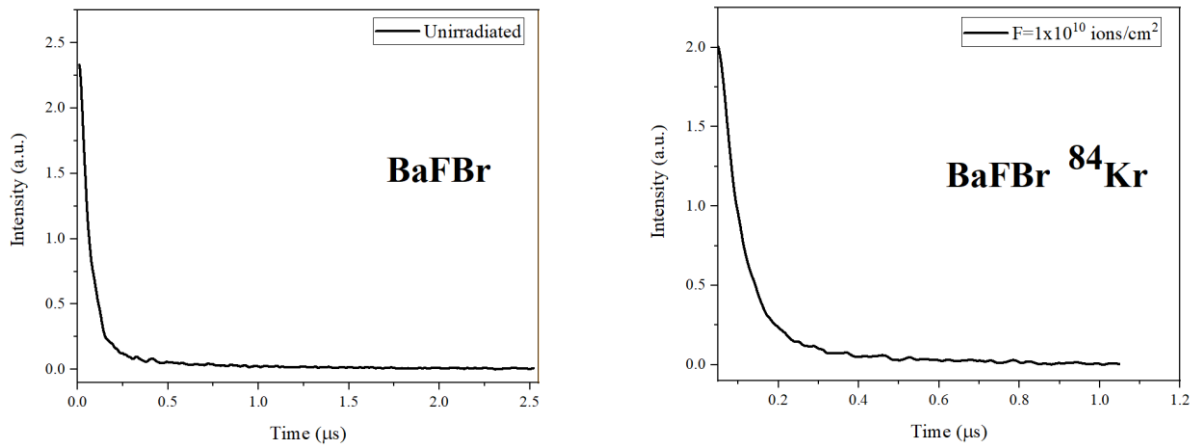

a) unirradiated sample b) fluence $1x10^{10}$ ions/cm^2 irradiated with ^{84}Kr

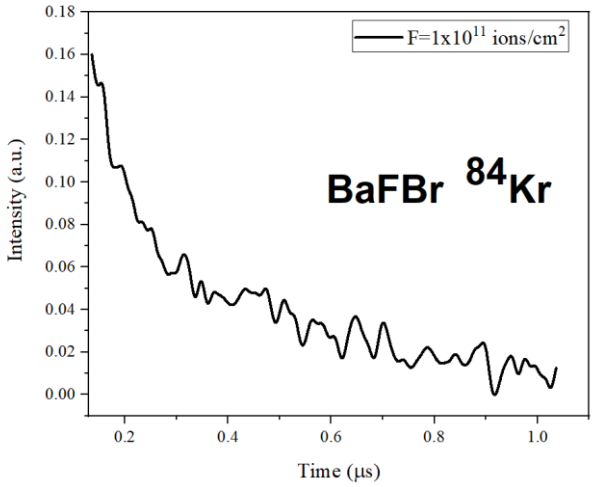

c) fluence $1x10^{11}$ ions/cm^2 irradiated with ^{84}Kr

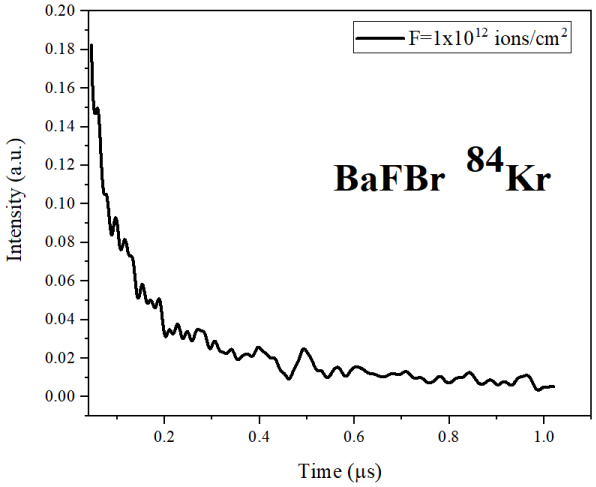

d) fluence $1x10^{12}$ ions/cm^2 irradiated with ^{84}Kr

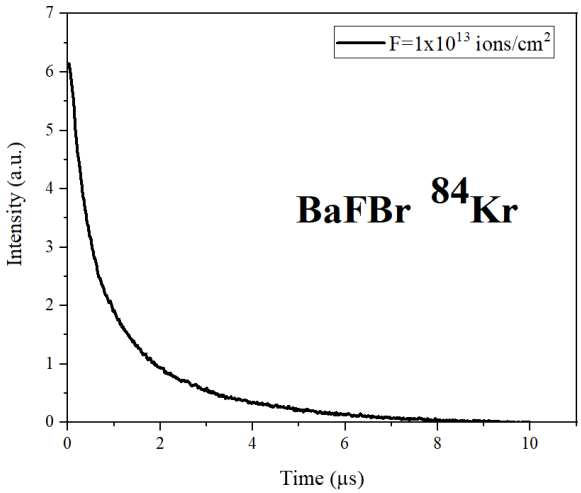

e) fluence $1x10^{13}$ ions/cm^2 irradiated with ^{84}Kr

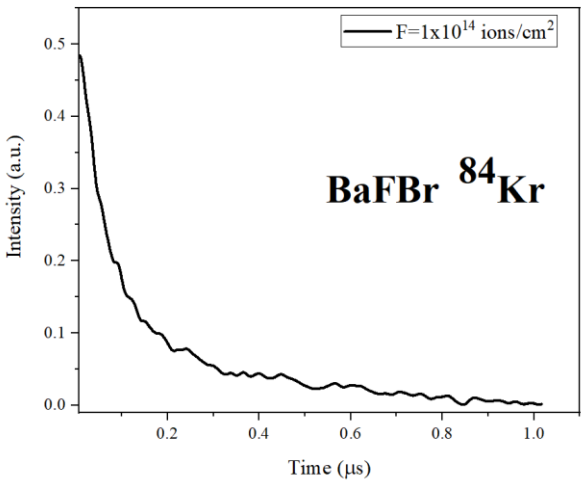

f) fluence $1x10^{14}$ ions/cm^2 irradiated with ^{84}Kr

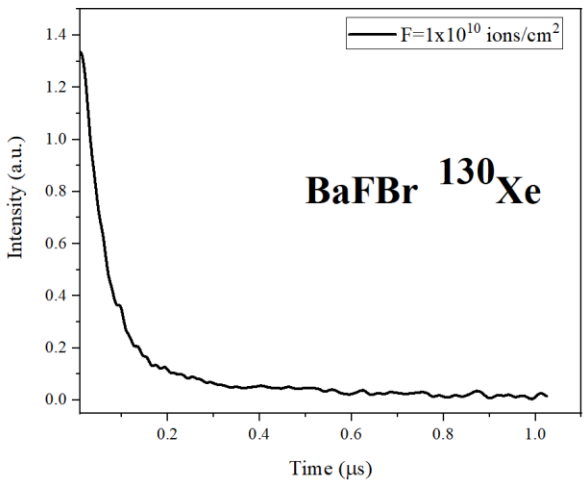

g) fluence $1x10^{10}$ ions/cm^2 irradiated with ^{130}Xe

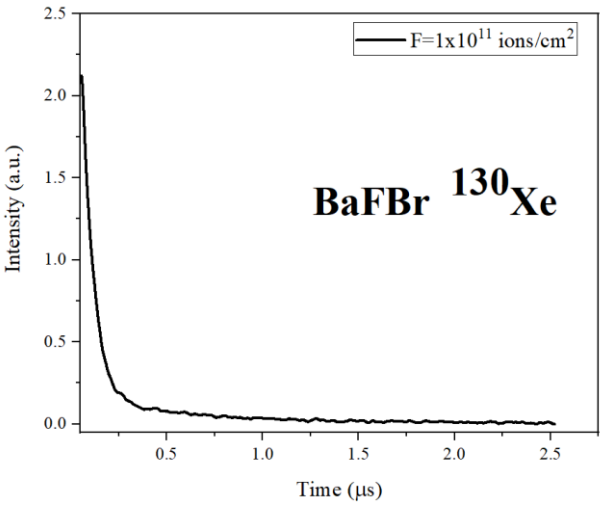

h) fluence $1x10^{11}$ ions/cm^2 irradiated with ^{130}Xe

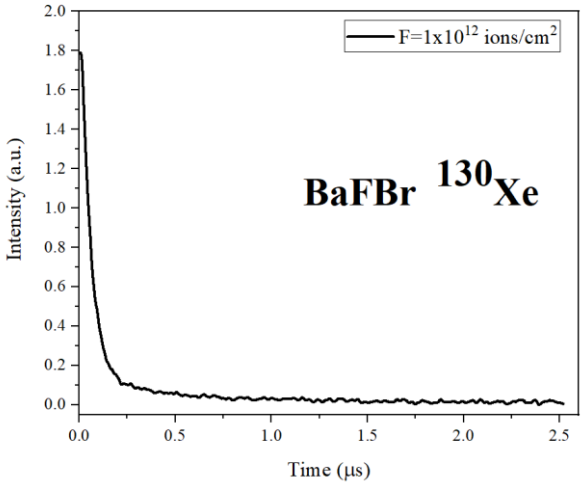

i) fluence 1x10^{12} ions/cm^2 irradiated with ^{130}Xe

Figure 4 – Kinetics of luminescence attenuation in 4.2 eV and 3.93 eV bands during pulsed electronic beam excitation of BaFBr crystal samples irradiated with ^{84}Kr ions with energy E=147 MeV, ^{130}Xe with energy E=227 MeV to fluences 1x10^{10} - 1x10^{12} ion/cm^2 of unalloyed BaFBr crystal, at room temperature

The band attenuation kinetics at 4.2 eV for BaFBr crystals unirradiated and irradiated by fast heavy ions with different energies is described by a set of two exponentials at T=296 K with different values of the characteristic attenuation time, recorded in the table below.

Table 1 – Parameters of PCL on ion type and fluence

Ion	(Φ), ion/cm^2	(λ), nm	(τ), max		(A)		S= τ x A		S_1/S_2 (%)
			τ_1	τ_2	A_1	A_2	S_1	S_2	
-	0	295	0.057	0.541	2.841	0.116	161.937	0.062756	99.96/0.04
^{84}Kr	1x10^{10}	295	0.057	0.571	4,853	0,146	276.621	0.083366	99.96/0.04
	1x10^{11}	295	0.062	0.721	0.817	0.108	0.05065	0.077868	39.42/60.58
	1x10^{12}	295	0.0478	0.266	0.274	0.065	0.01309	0.01729	43.11/56.89
	1x10^{13}	290	0.392	1.985	4.093	2.551	1.60446	5063.735	0.04/ 99.96
	1x10^{14}	310	0.059	0.467	0.454	0.125	0.02678	0.058375	31.45/68.55
^{130}Xe	1x10^{10}	295	0.051	0.498	1.656	0.114	0.08446	0.056772	59.81/40.19
	1x10^{11}	315	0.062	0.650	5.172	0.144	0.32066	0.0936	77.41/22.59
	1x10^{12}	295	0.054	0.555	2.135	0.103	0.11529	0.057165	66.85/33.15

The data presented in Table 1 show that the initial amplitude of the PCL attenuation kinetics is significantly larger for the fast component in the nanosecond range, regardless of the fluence in BaFBr crystals irradiated with krypton ions. In samples irradiated with 130Xe up to fluences 1011-1012 ions/cm2 there is an increase in the amplitude of the slow component. The fast component of the unirradiated sample gives a significant contribution to the percentage of the light-sum of the luminescence kinetics, starting from fluence1011 ion/cm2 at irradiation with 84Kr ions there is a shift towards the slow component. When irradiated with xenon ions, the fast component contributes to the light sum percentage.

4. Conclusions

PCL measurements of BaFBr crystals at room temperature revealed a dominant luminescence band at 4.2 eV, attributed to self-trapped excitons of bromine.

Irradiation with swift heavy ions (147 MeV Kr and 227 MeV Xe) at fluences ranging from 1×10^{10} to 1×10^{14} ions/cm² led to significant changes in luminescence intensity and decay kinetics.

At low fluences ($\leq1\times10^{11}$ ions/cm²), the fast nanosecond component dominated the emission with a light-sum contribution of up to 99.96%, while at higher fluences ($\geq1\times10^{13}$ ions/cm²), the slow microsecond component became more prominent, contributing up to 99.96% of the emission in some samples.

The shift in decay dynamics reflects increased defect formation and track overlap effects at higher ion fluences, which alter the excitonic recombination processes.

The study successfully addressed the research problem by demonstrating how ion irradiation affects both spectral and temporal PCL characteristics in BaFBr, revealing patterns of transition between fast and slow components based on irradiation dose.

These findings can be applied to optimize the performance of image plate phosphors and radiation detectors by tailoring the excitonic response through controlled ion modification.

The study was limited to room temperature measurements and selected ion species; future research could explore temperature-dependent behavior, other dopants, and extended dose ranges to further refine material performance.

Acknowledgments

This research was funded by Committee of Science of the Ministry of Science and Higher Education of the Republic of Kazakhstan (Grant No. AP19178510).

References

[1] H. Aichinger, S. Joite-Barfuß, J. Dierker, and M. Sabel, "Radiation exposure and image quality in X-ray diagnostic radiology: Physical principles and clinical applications," *Radiat. Expo. Image Qual. X-Ray Diagnostic Radiol. Phys. Princ. Clin. Appl.*, vol. 9783642112416, pp. 1–307, Nov. 2012, doi: 10.1007/978-3-642-11241-6/COVER.

[2] T. Peace, B. Subramanian, and P. Ravindran, "An experimental study on using a diagnostic computed radiography system as a quality assurance tool in radiotherapy," *Australas. Phys. Eng. Sci. Med. 2008 313*, vol. 31, no. 3, pp. 226–234, 2008, doi: 10.1007/BF03179349.

[3] J. Zimmermann, R. Kolb, S. Hesse, M. Schlapp, R. Schmechel, and H. Von Seggern, "Preparation-induced F-centre transformation in BaFBr : Eu2+," *J. Phys. D. Appl. Phys.*, vol. 37, no. 17, p. 2352, Aug. 2004, doi: 10.1088/0022-3727/37/17/002.

[4] D. Gonzales, S. Requena, S. Davis, and S. Williams, "Angular distribution of K-shell X-rays produced by 29 keV electrons incident on Ag," *Nucl. Instruments Methods Phys. Res. Sect. B Beam Interact. with Mater. Atoms*, vol. 269, no. 12, pp. 1333–1335, Jun. 2011, doi: 10.1016/J.NIMB.2011.04.004.

[5] D. R. Taikar, C. P. Joshi, and S. V. Moharil, "SrO:U6+ green light emitting phosphor," *J. Lumin.*, vol. 153, pp. 304–306, Sep. 2014, doi: 10.1016/J.JLUMIN.2014.03.057.

[6] G. Guérin *et al.*, "Testing the accuracy of a Bayesian central-dose model for single-grain OSL, using known-age samples," *Radiat. Meas.*, vol. 81, pp. 62–70, Oct. 2015, doi: 10.1016/J.RADMEAS.2015.04.002.

[7] A. Ohnishi and K. I. Kan'No, "Luminescence from self-trapped excitons in BaFI and BaFBr1–x Ix crystals," *Phys. status solidi*, vol. 245, no. 12, pp. 2815–2820, Dec. 2008, doi: 10.1002/PSSB.200844160.

[8] M. Batentschuk, A. Winnacker, K. Schwartz, and C. Trautmann, "Storage efficiency of BaFBr:Eu2+ image plates irradiated by swift heavy ions," *J. Lumin.*, vol. 125, no. 1–2, pp. 40–44, Jul. 2007, doi: 10.1016/J.JLUMIN.2006.08.023.

[9] H. Nanto and G. Okada, "Optically stimulated luminescence dosimeters: principles, phosphors and applications," *Jpn. J. Appl. Phys.*, vol. 62, no. 1, p. 010505, Nov. 2022, doi: 10.35848/1347-4065/AC9106.

[10] A. Akilbekov *et al.*, "The Effect of 147 MeV 84Kr and 24.5 MeV 14N Ions Irradiation on the Optical Absorption, Luminescence, Raman Spectra and Surface of BaFBr Crystals," *Cryst. 2024, Vol. 14, Page 480*, vol. 14, no. 6, p. 480, May 2024, doi: 10.3390/CRYST14060480.

Information about authors:
Daurzhan Kenbayev – PhD, Senior lecturer, Department of Physics and Informatics, Shakarim University, Semey, Kazakhstan, d.kenbayev@shakarim.kz
Elena Polisadova – Doctor of Physical and Mathematical Sciences, Professor, Department of Materials Science, National Research Tomsk Polytechnic University, Tomsk, Russian Federation. elp@tpu.ru
Alexei Shalayev – Candidate of Physics and Mathematics, Researcher at Laboratory "Physics of single crystals", Vinogradov Institute of Geochemistry , Irkutsk, Russian Federation, alshal@igc.irk.ru
Marina Konuhova – PhD, Researcher at Institute of Solid State Physics, University of Latvia, Riga, Latvia, mkonuhova@gmal.com

Author Contributions:
Daurzhan Kenbayev – data collection, testing, analysis, visualization, drafting.
Elena Polisadova – concept, methodology.
Alexei Shalayev – modeling, interpretation.
Marina Konuhova – resources, editing, funding acquisition.

Conflict of Interest: The authors declare no conflict of interest.

Use of Artificial Intelligence (AI): The authors declare that AI was not used.

Received: 20.02.2025
Revised: 27.03.2025
Accepted: 30.03.2025
Published: 31.03.2025